

## A MODEL FOR GRAVITATIONAL WAVE EMISSION FROM NEUTRINO-DRIVEN CORE-COLLAPSE SUPERNOVAE

JEREMIAH W. MURPHY<sup>1,6</sup>, CHRISTIAN D. OTT<sup>2,3,4</sup>, AND ADAM BURROWS<sup>5</sup>

<sup>1</sup> Department of Astronomy, University of Washington, Box 351580, Seattle, WA 98195-1580, USA; [jmurphy@astro.washington.edu](mailto:jmurphy@astro.washington.edu)

<sup>2</sup> Theoretical Astrophysics, Mailcode 350-17, California Institute of Technology, Pasadena, CA 91125, USA; [cott@tapir.caltech.edu](mailto:cott@tapir.caltech.edu)

<sup>3</sup> Niels Bohr International Academy, Niels Bohr Institute, Blegdamsvej 17, DK-2100 Copenhagen, Denmark

<sup>4</sup> Center for Computation and Technology, Louisiana State University, Baton Rouge, LA, USA

<sup>5</sup> Department of Astrophysical Sciences, Princeton University, Peyton Hall, Ivy Lane, Princeton, NJ 08544, USA; [burrows@astro.princeton.edu](mailto:burrows@astro.princeton.edu)

Received 2009 July 24; accepted 2009 November 2; published 2009 December 2

### ABSTRACT

Using a suite of progenitor models, neutrino luminosities, and two-dimensional simulations, we investigate the matter gravitational wave (GW) emission from postbounce phases of neutrino-driven core-collapse supernovae. These phases include prompt and steady-state convection, the standing accretion shock instability (SASI), and asymmetric explosions. For the stages before explosion, we propose a model for the source of GW emission. Downdrafts of the postshock-convection/SASI region strike the protoneutron star “surface” with large speeds and are decelerated by buoyancy forces. We find that the GW amplitude is set by the magnitude of deceleration and, by extension, the downdraft’s speed and the vigor of postshock-convective/SASI motions. However, the characteristic frequencies, which evolve from  $\sim 100$  Hz after bounce to  $\sim 300$ – $400$  Hz, are practically independent of these speeds (and turnover timescales). Instead, they are set by the deceleration timescale, which is in turn set by the buoyancy frequency at the lower boundary of postshock convection. Consequently, the characteristic GW frequencies are dependent upon a combination of core structure attributes, specifically the dense-matter equation of state (EOS) and details that determine the gradients at the boundary, including the accretion-rate history, the EOS at subnuclear densities, and neutrino transport. During explosion, the high frequency signal wanes and is replaced by a strong low frequency,  $\sim 10$ s of Hz, signal that reveals the general morphology of the explosion (i.e., prolate, oblate, or spherical). However, current and near-future GW detectors are sensitive to GW power at frequencies  $\gtrsim 50$  Hz. Therefore, the signature of explosion will be the abrupt reduction of detectable GW emission.

*Key words:* dense matter – equation of state – gravitational waves – hydrodynamics – instabilities – shock waves – supernovae: general – turbulence

*Online-only material:* color figures

### 1. INTRODUCTION

Core-collapse supernovae (CCSNe) are among the most energetic events in the universe; they herald the birth of neutron stars and black holes, are a major site for nucleosynthesis, influence galactic dynamics, trigger further star formation, and are prodigious emitters of neutrinos and gravitational waves (GWs). Hence, it is important to understand the mechanism of explosion, yet the details have remained elusive for many decades.

GWs promise to be important diagnostics for revealing the secrets of the CCSN mechanism. Despite the elusiveness of the CCSN problem, current multi-dimensional simulations show several promising mechanisms. Whether the solution is the convection/SASI-aided neutrino mechanism (Marek & Janka 2009; Murphy & Burrows 2008b), the acoustic mechanism (Burrows et al. 2006, 2007c), or magnetohydrodynamic (MHD) jets (Burrows et al. 2007b; Dessart et al. 2008; and the references therein), viable explosion mechanisms for all but the least massive of massive stars (Kitaura et al. 2006; Burrows et al. 2007a) appear fundamentally multi-dimensional. Because photons couple strongly with matter, the mechanism is obscured by many solar masses and traditional means of observation are limited. However, neutrinos and GWs interact very weakly with matter and provide a clear view into the dynamics of the mechanism. Unlike neutrinos, GWs are emitted (at lowest order)

by time-changing quadrupole mass/energy motions. Therefore, the multi-dimensional mechanisms for CCSNe are expected to be a significant source of GWs, which will in turn provide a diagnostic into their multi-dimensional nature.

This important connection between CCSNe and GWs was recognized quite early (for a comprehensive review of GWs and CCSNe, see Ott 2009b). Most early investigations were limited to the collapse and bounce of rapidly rotating iron cores (Müller 1982; Mönchmeyer et al. 1991; Yamada & Sato 1995; Zwerger & Müller 1997; Dimmelmeier et al. 2002; Kotake et al. 2003; Ott et al. 2004). Current investigations, which focus on these early phases and rapid rotation, use two-dimensional (2D) or three-dimensional (3D) simulations, conformally flat or full general relativity, finite-temperature nuclear equations of state (EOS), and deleptonization during collapse (Dimmelmeier et al. 2007, 2008; Ott et al. 2007). However, the rotation rates necessary for GWs with sizeable amplitudes are likely to obtain in only  $\sim 1\%$  of the massive star population (Heger et al. 2005; Hirschi et al. 2004; Woosley & Heger 2006; Ott et al. 2006b).

Another set of studies has focused on the GW signatures of postbounce phases and dynamics. These include convection in the protoneutron star (PNS) and in the postshock region (Burrows & Hayes 1996; Müller & Janka 1997; Müller et al. 2004; Marek et al. 2009), the standing accretion shock instability (SASI; Kotake et al. 2007, 2009; Marek et al. 2009), PNS internal  $g$ -modes associated with an acoustic mechanism for explosion (Burrows et al. 2006, 2007c; Ott et al. 2006a),

<sup>6</sup> NSF Astronomy and Astrophysics Postdoctoral Fellow.

rapid rotation in the context of MHD jets (Kotake et al. 2004; Obergaulinger et al. 2006), or asymmetric explosion and neutrino emission which lead to a long-term nonzero GW strain, or “memory” (Braginskii & Thorne 1987; Burrows & Hayes 1996; Müller & Janka 1997; Müller et al. 2004). Each signature is associated with the three possible explosion mechanisms, and Ott (2009a) suggests that their GW characteristics may help to distinguish which mechanism obtains in a particular supernova.

In this paper, we address neither the GW signatures of PNS  $g$ -modes nor rapid rotation but focus on the GWs from the postbounce phases of the neutrino mechanism. The bounce shock is quickly stalled by nuclear dissociation, electron capture, and neutrino losses (Mazurek 1982; Bruenn 1985, 1989) and leaves a negative entropy gradient. This leads to an initial, short-lived ( $\lesssim 50$  ms) phase of strong convective overturn, prompt convection (Burrows & Fryxell 1992), and an associated burst of GWs (Marek et al. 2009; Ott 2009b). More than two decades ago, Wilson (1985) and Bethe & Wilson (1985) suggested that a fraction of the neutrinos being emitted from depth ( $\lesssim 100$  km) would be recaptured in the gain region ( $\gtrsim 100$  km), reviving the stalled shock into explosion. However, detailed one-dimensional (1D) simulations have shown that this mechanism, the neutrino mechanism, fails in 1D (Liebendörfer et al. 2001b, 2001a; Rapp & Janka 2002; Buras et al. 2003; Thompson et al. 2003; Liebendörfer et al. 2005), except for the least massive of the massive stars (Kitaura et al. 2006; Burrows et al. 2007a). Recent 2D simulations that are subject to aspherical instabilities, specifically postshock convection, which is driven by neutrino heating in the gain region and the SASI, suggest that the neutrino mechanism may yet succeed, though it fails in 1D (Herant et al. 1994; Janka & Müller 1995; Burrows et al. 1995; Janka & Müller 1996; Burrows et al. 2007c; Kitaura et al. 2006; Buras et al. 2006b, 2006a; Marek & Janka 2009; Ott et al. 2008; Murphy & Burrows 2008b). In particular, Murphy & Burrows (2008b) parameterized the neutrino luminosity and found that the critical neutrino luminosity for explosions is lower in 2D simulations compared to 1D. These results suggest that asymmetries are not only important for the production of GWs, but also for the success of the neutrino mechanism.

PNS convection (see Dessart et al. 2006 and the references therein) and postshock convection (Burrows et al. 1995; Janka & Müller 1996) have been recognized as an important ingredient in CCSNe for many decades. However, it was only recently that the SASI has been recognized as a distinct instability that augments neutrino-driven convection in the gain region (Blondin et al. 2003). The mechanism responsible for this instability is debated to be either an advective-acoustic cycle (Foglizzo & Tagger 2000; Foglizzo 2001, 2002, 2009; Blondin et al. 2003; Ohnishi et al. 2006; Foglizzo et al. 2007; Iwakami et al. 2008; Scheck et al. 2008; Yamasaki & Foglizzo 2008; Sato et al. 2009) or purely acoustic cycle (Blondin & Mezzacappa 2006; Laming 2007), though recent linear and nonlinear analyses of simple models suggest that the advective-acoustic cycle is responsible (Sato et al. 2009; Foglizzo 2009). An additional complication is that it is hard to disentangle the effects of the SASI from those of postshock convection. They both occupy the same region, reach nonlinear saturation quickly, and likely influence each other’s nonlinear motions. Given the recent recognition of the SASI, it is no wonder that few have investigated fully the GW characteristics of the convection/SASI-aided neutrino mechanism (Kotake et al. 2007, 2009; Marek et al. 2009).

Using simulations performed with the 2D radiation-hydrodynamics code VULCAN/2D, Ott et al. (2006a) described

some GW signatures of the SASI, but primarily focused on the GW emission from strong core  $g$ -modes. Kotake et al. (2007) were the first to specifically investigate the GW signature of the SASI in 2D. To expedite calculations, they made several assumptions. Their initial conditions were derived from a steady-state approximation of the postshock structure and not from stellar evolution calculations. They used an inner boundary at 50 km and kept the density at this boundary constant at  $10^{11}$  g cm $^{-3}$ . Although they used a relativistic-mean-field EOS (Shen et al. 1998), they approximated the effects of neutrino interactions with local heating and cooling terms and assumed a fixed accretion rate at the grid outer boundary. Even though they omitted the PNS and proper neutrino transport, they estimated the GW emission from matter and neutrinos, and found that the GW amplitudes due to asymmetric neutrino emission are  $\sim 100$  times that of matter, but at low frequency and hence lower power. They also found that the matter GW signal grows as the SASI enters the nonlinear phase and that the characteristic frequency from the matter GW emission is  $\sim 100$  Hz. Interestingly, they did not find a signature of explosion that is distinct from steady-state convection and/or SASI. More recently, Kotake et al. (2009) used a similar simulation approach in 3D simulations and employed a ray-tracing technique to estimate the asymmetric neutrino emission, obtaining a neutrino GW signal comparable in magnitude to the matter signal. Though one might expect higher neutrino luminosities to result in stronger convection/SASI motion, they found that the strength of the GW emission does not correlate with neutrino luminosity. Rather, they concluded that the stochastic motions of the SASI prevents such a correlation between GW strength and neutrino luminosity.

Marek et al. (2009) use different approximations to investigate the GW characteristics in 2D simulations and obtain different results. They use a compressible liquid-drop model EOS as well as relativistic-mean-field and a Brueckner–Hartree–Fock EOSs, 1D ray-by-ray neutrino transport, initial conditions derived from stellar evolution calculations, a pseudo-GR gravitational potential that mimics the effects of GR in spherical symmetry, and an inner boundary at  $\sim 2$  km. With these more realistic assumptions, they obtain matter GW amplitudes that are only half of the neutrino GW signal. Just after bounce, they report characteristic frequencies of  $\sim 100$  Hz, similar to Kotake et al. (2007). However, Marek et al. (2009) associate these frequencies with the short-lived prompt convection rather than general SASI motions. When nonlinear SASI begins in earnest, augmenting the nonradial motions of neutrino-driven convection, they report that the GW power peaks at  $\sim 300$ – $800$  Hz and attribute the source of GWs to vigorous SASI and convective motions above and below the neutrinosphere. A primary conclusion of their work is that the peak frequency depends upon the compactness of the PNS and, by extension, the dense-matter EOS, in that softer EOSs result in higher frequencies.

Both groups state that GWs are generated by convective overturns and sloshing motions of the SASI. In fact, Kotake et al. (2009) make direct reference to overturn and sloshing timescales for the origin of GW characteristic frequencies. Marek et al. (2009) also discuss these timescales in the context of prompt and PNS convection, but they go further to suggest that asymmetric motions in the neutrino heating and cooling layers stirred by vigorous SASI funnels and convective overturn are significant sources of GW emission as well. However, neither quantitatively define the relevant timescales, nor give support for these associations. In fact, most timescale definitions in the literature associated with postshock convection and

the SASI give frequencies ( $\sim 30\text{--}100$  Hz) that are quite low (Burrows et al. 2007b; Scheck et al. 2008; Marek & Janka 2009) compared to the frequencies ( $\gtrsim 300$ ) associated with peak GW power. This discrepancy suggests that another timescale is relevant in determining the characteristic GW frequency. So, here we ask several obvious questions. What determines the characteristic frequencies and amplitudes, how do these change with progenitor mass and neutrino luminosity, and what is the GW signature of explosion?

Theoretical GW signals that reproduce observations with fidelity will require 3D radiation-hydrodynamic simulations. However, such simulations are computationally expensive and prohibit systematic studies of the important physics. In the spirit of Murphy & Burrows (2008b), we simulate simplified models that nevertheless retain the important physics, and allow one to adjust key parameters. Our approach is a compromise between Kotake et al. (2007) and Marek et al. (2009). Like Marek et al. (2009), we use recent core-collapse progenitor models (Woosley & Heger 2007) as initial conditions and a finite-temperature relativistic-mean-field EOS. Rather than studying the effects of the EOS, we perform simulations with four progenitor models: 12, 15, 20, and  $40 M_{\odot}$ . To avoid waiting six months (or more) for a single simulation, we compromise on the neutrino transport and use local heating and cooling approximations similar to Kotake et al. (2007). Finally, we use spherical Newtonian gravity. Though these assumptions prevent accurate models, simulations can be calculated in a timely manner that include important qualitative features of core collapse. Because we do not use neutrino transport, but a simple local heating and cooling algorithm, we calculate the GW signal due to asymmetric mass motions and not asymmetric neutrino emission. Since the neutrino and matter GW signals are emitted at low and high frequencies, respectively, and GW detectors are sensitive to the high frequencies, calculating the matter GW signal is sufficient for predicting GW observations in the near future.

In the following sections, we present a systematic parameterization of progenitor mass and neutrino luminosity in the neutrino mechanism context. In Section 2, we present the basic equations, assumptions, and numerical techniques. In Section 3, we present and discuss the results of this paper. For GW extraction, we consider the quadrupole formula of the slow-motion, weak-field approximation (Section 3.1). In Section 3.2, we describe the generic features of GW emission, which include prompt convection, postshock convection, SASI, and asymmetric explosions. In Section 3.3, we show energy spectra and spectrograms, describing the characteristic frequencies and their dependence on progenitor mass and time of explosion. In Section 3.4, we consider the characteristic frequencies and amplitudes of the downdrafts striking the PNS “surface,” where they decelerate due to buoyancy force and show that these match the characteristic frequencies and amplitudes of the GWs. Finally, in Section 4, we summarize our results and suggest a program for further investigation.

## 2. NUMERICAL TECHNIQUES

### 2.1. Hydrodynamics

For the 2D simulations presented in this paper, we use BETHE-hydro (Murphy & Burrows 2008a, 2008b), an Arbitrary Lagrangian–Eulerian (ALE) hydrodynamics code. The basic equations of hydrodynamics are the conservation of mass,

momentum, and energy:

$$\frac{d\rho}{dt} = -\rho \nabla \cdot \mathbf{v}, \quad (1)$$

$$\rho \frac{d\mathbf{v}}{dt} = -\rho \nabla \Phi - \nabla P, \quad (2)$$

and

$$\rho \frac{d\varepsilon}{dt} = -P \nabla \cdot \mathbf{v} + \rho(\mathcal{H} - \mathcal{C}), \quad (3)$$

where  $\rho$  is the mass density,  $\mathbf{v}$  is the fluid velocity,  $\Phi$  is the gravitational potential,  $P$  is the isotropic pressure,  $\varepsilon$  is the specific internal energy, and  $d/dt = \partial/\partial t + \mathbf{v} \cdot \nabla$  is the Lagrangian time derivative. In this work, the neutrino heating,  $\mathcal{H}$ , and cooling,  $\mathcal{C}$ , terms in Equation (3) are assumed to be

$$\mathcal{H} = 1.544 \times 10^{20} L_{\nu_e} \left( \frac{100 \text{ km}}{r} \right)^2 \left( \frac{T_{\nu_e}}{4 \text{ MeV}} \right)^2 \left[ \frac{\text{erg}}{\text{g s}} \right], \quad (4)$$

in which we assume the free-streaming limit,<sup>7</sup> and

$$\mathcal{C} = 1.399 \times 10^{20} \left( \frac{T}{2 \text{ MeV}} \right)^6 \left[ \frac{\text{erg}}{\text{g s}} \right]. \quad (5)$$

Note that these approximations for heating and cooling by neutrinos (Bethe & Wilson 1985; Janka 2001) depend upon local quantities and predefined parameters. They are  $\rho$ , temperature ( $T$ ), the distance from the center ( $r$ ), the electron–neutrino temperature ( $T_{\nu_e}$ ), and the electron–neutrino luminosity ( $L_{\nu_e}$ ), which we give in units of  $10^{52} \text{ erg s}^{-1}$ . By using Equations (4) and (5), we gain considerable time savings by approximating the effects of detailed neutrino transport. For all simulations, we set  $T_{\nu_e} = 4 \text{ MeV}$ . In Equation (4), it has been assumed that  $L_{\nu_e} = L_{\bar{\nu}_e}$  and that the mass fractions of protons and neutrons sum to one. Therefore, the sum of the electron- and anti-electron–neutrino luminosities is  $L_{\nu_e \bar{\nu}_e} = 2L_{\nu_e}$ . Closure for Equations (1)–(3) is obtained with the finite-temperature nuclear EOS of Shen et al. (1998) to which we have added the effects of photons, electrons, and positrons. As such, the EOS has the following dependencies:

$$P = P(\rho, \varepsilon, Y_e), \quad (6)$$

where  $Y_e$  is the electron fraction. Given this  $Y_e$  dependence, we also solve the equation:

$$\frac{dY_e}{dt} = \Gamma_e, \quad (7)$$

where  $\Gamma_e$  is the net rate of  $Y_e$  change.

The heating and cooling functions, Equations (4) and (5), are valid for optically thin regions only. To mimic the reduction in heating and cooling at depth where the PNS is opaque to neutrinos, we multiply by  $e^{-\tau_{\text{eff}}}$ . In 1D simulations, the effective optical depth for electron- and anti-electron-type neutrinos is calculated by

$$\tau_{\text{eff}} = \int_r^{\infty} \kappa_{\text{eff}}(r) dr, \quad (8)$$

<sup>7</sup> The neutrino distribution is entirely forward peaked and the flux factor is one.

where the effective opacity,  $\kappa_{\text{eff}}$  is given by Equation (15) or (16) of Janka (2001), which we reproduce without derivation:

$$\kappa_{\text{eff}}(r) \approx 1.5 \times 10^{-7} X_{n,p} \left( \frac{\rho}{10^{10} \text{ g cm}^{-3}} \right) \left( \frac{T_{\nu_e}}{4 \text{ MeV}} \right)^2 \text{ cm}^{-1}, \quad (9)$$

where  $X_{n,p}$ , the composition weighting, is  $\sim \frac{1}{2}(Y_n + Y_p)$  and  $Y_n$  and  $Y_p$  are the number fractions of free neutrons and protons. Because the radial density profile after bounce is monotonic and, to good approximation, a series of power laws,  $\tau_{\text{eff}}$  is roughly a function of local density only. We use our 1D simulations to calibrate this  $\tau$ - $\rho$  relationship and parameterize  $\tau$  as function of  $\rho$  for the 2D simulations.

The heating and cooling terms are set to zero during collapse and are turned on after bounce. We have experimented with several methods to do this, but find that they give similar results provided that these terms “turn on” within a few milliseconds of bounce. For convenience, we include heating and cooling once the maximum value of  $\tau$  is greater than 100.

Using BETHE-hydro (Murphy & Burrows 2008a), we solve Equations (1)–(3) in two dimensions by the ALE method. To advance the discrete equations of hydrodynamics by one time step, ALE methods generally use two operations, a Lagrangian hydrodynamic step followed by a remap. The structure of BETHE-hydro’s hydrodynamic solver is designed for arbitrary-unstructured grids, and the remapping component offers control of the time evolution of the grid. Taken together, these features enable the use of time-dependent arbitrary grids to avoid some unwanted features of traditional grids.

For the calculations presented in this paper, we use this flexibility to avoid the coordinate singularity of spherical grids in two dimensions. While spherical grids are generally useful for core-collapse simulations, the convergence of grid lines near the center places extreme constraints on the time step via the Courant–Friedrichs–Levy condition. A common remedy is to simulate the inner  $\sim 10$  km in 1D or to use an inner boundary condition. Another approach, which has been used in VULCAN/2D simulations (Livne 1993; Livne et al. 2004; Burrows et al. 2007c), is to avoid the singularity with a grid that is pseudo-Cartesian near the center and smoothly transitions to a spherical grid at larger radii.

In this paper, we use a similar grid, the butterfly mesh (Murphy & Burrows 2008a, 2008b) interior to 34 km and a spherical grid exterior to this radius. See Murphy & Burrows (2008a) for an example. For all  $180^\circ$  simulations, the innermost pseudo-rectangular region is 50 by 100 zones, and the region that transitions from Cartesian to spherical geometry has 50 radial zones and 200 angular zones. The outermost spherical region has 200 angular zones and 500 radial zones that are logarithmically spaced between 34 km and 8000 km in most cases. Due to EOS constraints, the outer boundary goes out to 6000 km for the  $12 M_\odot$  model. The butterfly portion has an effective radial resolution of 0.34 km with the shortest cell edge being 0.28 km. In 2D simulations, we do not remap every time step. Since the time step is limited by the large sound speeds in the PNS core, we can afford to perform several Lagrangian hydrodynamic solves before remapping back to the original grid. By remapping rarely, we gain considerable savings in computational time.

We make several approximations to expedite the calculations. For one, gravity is calculated via  $\vec{g} = -GM_{\text{int}}/r^2$ , where  $M_{\text{int}}$  is the mass interior to the radius  $r$ . Furthermore, since we do not solve the neutrino transport equations, we do not obtain electron/positron capture and emission rates, which are

necessary for self-consistent  $Y_e$  profiles and evolution. Instead, we use a  $Y_e$  versus  $\rho$  parameterization that is quantitatively accurate during collapse and gives the correct qualitative trends after bounce. Liebendörfer (2005) observed that 1D simulations including neutrino transport produce  $Y_e$  values during collapse that are essentially a function of density alone. This allows for a parameterization of  $Y_e$  as a function of  $\rho$ . To change  $Y_e$ , we use results of 1D SESAME (Burrows et al. 2000; Thompson et al. 2003) simulations to define the function  $Y_e(\rho)$ , and we employ the prescription of Liebendörfer (2005) to calculate local values of  $\Gamma_e$ . Though this prescription is most appropriate during collapse, we also apply it after bounce to continue deleptonizing postshock material at later times. While this is not entirely consistent with our heating and cooling prescription, the most important effects of deleptonization are included without the need for expensive, detailed neutrino transport.

The approximations for neutrino–matter interactions, electron capture rates, and gravity give simulations that reproduce the primary features of the core-collapse problem. These include a PNS, a stalled shock at  $\sim 200$  km, a gain radius at  $\sim 100$  km (that divides the gain region above with net heating from the cooling region below), prompt convection, PNS convection from  $\sim 20$  to  $\sim 45$  km, postshock convection, and the SASI. While the  $Y_e$ - $\rho$  parameterization is designed to give the proper  $Y_e$  profile during collapse, we do not reproduce the  $Y_e$  trough at later times that extends from  $\sim 40$  km to the shock (e.g., Dessart et al. 2006). Dessart et al. (2006) conclude that the negative lepton gradient from  $\sim 15$  to  $\sim 30$  km in simulations employing consistent neutrino transport drives the PNS convection. In our simulations, PNS convection is driven by a negative entropy gradient. Although 1D simulations that solve neutrino transport more consistently show a similar negative entropy gradient, the depth and width are smaller in those simulations (compare Figures 13 and 6 of Murphy & Burrows 2008b; Liebendörfer et al. 2005). Furthermore, our PNS convection velocities are roughly a factor of 2 larger than those obtained by Dessart et al. (2006). In summary, while we obtain a PNS convective region, our PNS convection is predominantly driven by an entropy gradient rather than by a negative lepton gradient and is more extended and vigorous compared to more realistic calculations. However, we show in later sections that though the GW signal due to PNS convection is important, it is not an overwhelmingly dominant feature of GW emission from CCSNe. Therefore, the differences in PNS convection should not change the qualitative conclusions of this paper.

## 2.2. Progenitor Models

As initial conditions, we use the 12, 15, 20, and  $40 M_\odot$  core-collapse progenitor models of Woosley & Heger (2007), where these masses correspond to the zero-age-main-sequence (ZAMS) masses. In Figure 1, we plot the mass accretion rate versus time after bounce (solid black lines) for each of these models. In general, because the more massive progenitors have extended core structures, the accretion rates for them are higher at a given time. Since higher accretion rates require larger neutrino luminosities for successful explosions (Murphy & Burrows 2008b), this translates into higher critical neutrino luminosities for the more massive progenitors. In fact, if we assume that only the neutrino mechanism leads to explosion, the required neutrino luminosity for successful explosions of the  $40 M_\odot$  progenitor is so high,  $\gtrsim 10^{53} \text{ erg s}^{-1}$ , we doubt that it will explode at all and suspect that the non-explosive simulation using  $L_{\nu_e} = 6 \times 10^{52} \text{ erg s}^{-1}$  represents the likely outcome of

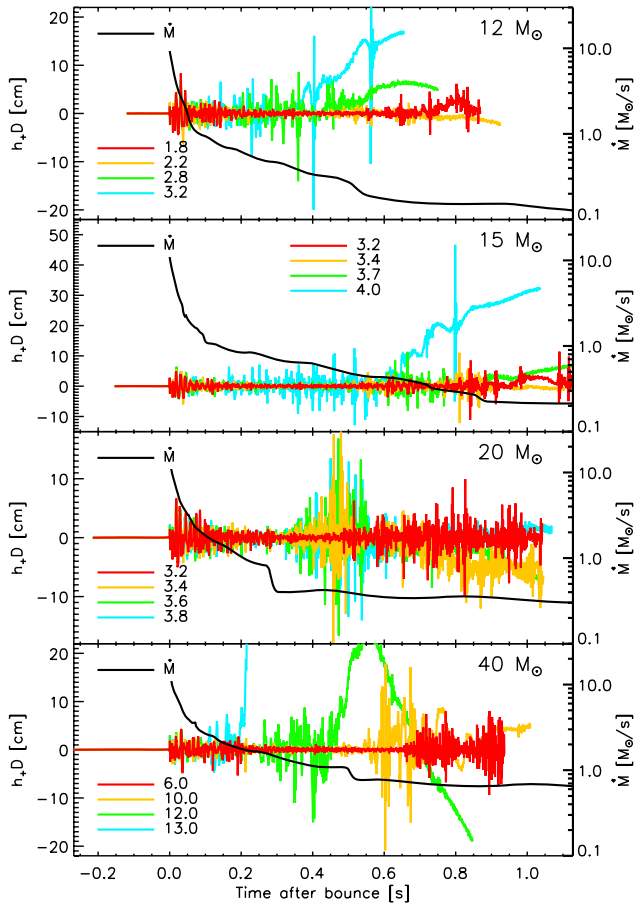


**Figure 1.** Dimensionless GW strain  $h_+$  times the distance,  $D$ , vs. time after bounce for the suite of simulations presented in this paper. Each panel represents a single progenitor model and the curves are labeled by  $L_{v_e}$  in units of  $10^{52} \text{ erg s}^{-1}$ . The accretion rates (in  $M_\odot \text{ s}^{-1}$ ) at the stalled shock of non-exploding models are shown for comparison. All models show GW features associated with prompt convection, postshock convection, SASI, and explosion with the exception that the run using  $M = 40 M_\odot$  and  $L_{v_e} = 6.0 \times 10^{52} \text{ erg s}^{-1}$  does not explode. See Figure 2 for a sample GW strain evolution with these features labeled. In general, lower luminosity runs develop the strong SASI motions and explosions at later times, but all runs saturate at roughly similar amplitudes ( $h_+ D \sim 10 \text{ cm}$ ). In the simulations using the  $20 M_\odot$  progenitor, the accretion of the interface between the progenitor’s Si and O burning shells through the shock causes a sudden drop in accretion rate. This initiates strong convective/SASI motions in the highest luminosity runs (3.4, 3.6, and 3.8) and suggests a means to use GW signals to probe the location of this interface. However, this feature is unique to the runs using the  $20 M_\odot$  progenitor.

(A color version of this figure is available in the online journal.)

core collapse for the  $40 M_\odot$  progenitor. In general, these trends with progenitor mass will translate to trends in the GW signal, which we discuss in forthcoming sections.

Although core structure follows a general trend with the progenitor’s ZAMS mass, the correlation is known to be somewhat chaotic (Woosley et al. 2002). For example, a substantial drop in the  $20 M_\odot$  model’s accretion rate corresponding to the interface between the Si and O burning shells temporarily reduces the accretion below even the 12 and  $15 M_\odot$  progenitors at  $\sim 300 \text{ ms}$  past bounce. This has consequences for the development of the SASI, explosion, and the GW signal.

### 3. RESULTS

#### 3.1. GW Extraction and Analysis

We extract the GW signal from our hydrodynamic simulations via the slow-motion, weak-field formalism (e.g., Misner et al.

1973) and consider the dominant mass-quadrupole only. In this approximation, the GW field is directly proportional to the transverse-traceless (TT) part of the second time derivative of the reduced mass-quadrupole tensor  $\mathcal{F}_{jk}$ . Specifically,

$$h_{jk}^{TT}(t, \mathbf{x}) = \frac{2}{c^4} \frac{G}{D} \left[ \frac{d^2}{dt^2} \mathcal{F}_{jk}(t - D/c) \right]^{TT}, \quad (10)$$

and

$$\mathcal{F}_{jk} = \int \rho \left( x^j x^k - \frac{1}{3} \delta^{jk} x_i x^i \right) d^3 x. \quad (11)$$

In the above,  $D$  is the observer distance to the source of emission. All other variables and constants have their usual meaning and the Einstein sum convention is assumed. For numerical convenience, we employ the so-called first-moment-of-momentum-divergence (FMD) recast of Equation (10) proposed by Finn & Evans (1990), which employs the continuity equation to remove one time derivative. In axisymmetry,  $\mathcal{F}_{ij}$  reduces to one independent component ( $\mathcal{F}_{zz}$ ), and, adapted to spherical coordinates, the FMD formula for its first time derivative reads

$$\frac{d}{dt} \mathcal{F}_{zz} = \frac{8\pi}{3} \int_{-1}^1 d \cos \theta \int_{r_1}^{r_2} dr r^3 \rho \cdot \left[ P_2(\cos \theta) v_r + \frac{1}{2} \frac{\partial}{\partial \theta} P_2(\cos \theta) v_\theta \right], \quad (12)$$

where  $P_2(\cos \theta)$  is the second Legendre polynomial in  $\cos \theta$ , and  $v_r$  and  $v_\theta$  are the fluid velocities in the radial and lateral direction, respectively. The axisymmetric<sup>8</sup> GW strain  $h_+ = h_{\theta\theta}$  (dropping the TT superscript) is then given by

$$h_+ = \frac{3}{2} \frac{G}{D c^4} \sin^2 \alpha \frac{d^2}{dt^2} \mathcal{F}_{zz}, \quad (13)$$

where  $\alpha$  is the angle between the symmetry axis and the line of sight of the observer and the second time derivative is obtained via straightforward differentiation.<sup>9</sup> For our simulations, this approach yields good results and we do not find it necessary to employ the modification of Equation (10) proposed by Blanchet et al. (1990) that removes both time derivatives, but introduces a sensitive dependence on derivatives of the Newtonian gravitational potential, which we treat only in spherical fashion.

In our analysis of the GW signature, we not only consider the dimensionless GW strain  $h_+$ , but also compute the total emitted energy in GWs, given by

$$E_{\text{GW}} = \frac{3}{10} \frac{G}{c^5} \int_0^t \left( \frac{d^3}{dt^3} \mathcal{F}_{zz} \right)^2 dt, \quad (14)$$

and the GW spectral energy density via

$$\frac{dE_{\text{GW}}}{df} = \frac{3}{5} \frac{G}{c^5} (2\pi f)^2 |\tilde{A}|^2, \quad (15)$$

where  $\tilde{A}$  denotes the Fourier transform of  $A \equiv \frac{d^2}{dt^2} \mathcal{F}_{zz}$  computed via

$$\tilde{A}(f) = \int_{-\infty}^{\infty} A(t) e^{-2\pi i f t} dt. \quad (16)$$

<sup>8</sup> Note that in axisymmetry  $h_\times = 0$  everywhere and  $h_+$  is nonzero only away from the axis of symmetry of the system.

<sup>9</sup> Note that due to a misprint in Equation (38) of Finn & Evans (1990) their expression is a factor of 2 smaller than our expression in Equation (13).

At this point, it is useful to define for future reference the dimensionless characteristic GW strain (Flanagan & Hughes 1998), in terms of the GW spectral energy density,

$$h_{\text{char}} = \sqrt{\frac{2 G}{\pi^2 c^3} \frac{1}{D^2} \frac{dE_{\text{GW}}}{df}}. \quad (17)$$

For signals with relatively stable frequencies and amplitudes, Fourier transforms and their energy spectra are adequate frequency analysis tools. However, for signals with time-varying amplitudes and frequencies, a short-time Fourier transform (STFT) is more appropriate. The STFT of  $A(t)$  is

$$\tilde{S}(f, \tau) = \int_{-\infty}^{\infty} A(t) H(t - \tau) e^{-2\pi i f t} dt, \quad (18)$$

where  $\tau$  is the time offset of the window function,  $H(t - \tau)$ . We use the Hann window function:

$$H(t - \tau) = \begin{cases} \frac{1}{2} \left(1 + \cos\left(\frac{\pi(t-\tau)}{\delta t}\right)\right) & \text{for } |t - \tau| \leq \frac{\delta t}{2} \\ 0 & \text{for } |t - \tau| > \frac{\delta t}{2} \end{cases}, \quad (19)$$

where  $\delta t$  is the width of the window function. The analog of the energy spectrum of the Fourier transform is the spectrogram,  $|\tilde{S}(f, \tau)|^2$ . Using the spectrogram, we define an analog to the energy emission per frequency interval (Equation (15)):

$$\frac{dE_{\text{GW}}^*}{df}(f, \tau) = \frac{3 G}{5 c^5} (2\pi f)^2 |\tilde{S}(f, \tau)|^2. \quad (20)$$

We emphasize that the GW strains reported in this paper are based upon matter motions alone and do not include the low-frequency signal that results from asymmetric neutrino emission (Burrows & Hayes 1996; Müller & Janka 1997). Accurate calculations of asymmetric neutrino emission require multi-dimensional, multi-angle neutrino transport to capture the true asymmetry of the neutrino radiation field (see, e.g., Ott et al. 2008). Our choice to parameterize the effects of neutrino transport by local heating and cooling algorithms is based upon assumptions of transparency, which ignore diffusive effects and would exaggerate the asymmetries and resulting GWs. For example, Kotake et al. (2007) estimated the neutrino GW signal using a similar heating and cooling parameterization and obtained GW strain amplitudes that are  $\sim 100$  times the matter GW signal. However, with an improved ray-tracing-based method, the same authors find much smaller amplitudes that are larger than those due to matter motions by only a factor of a few (Kotake et al. 2009). This is in agreement with the GW estimates of Marek et al. (2009) who used 1D ray-by-ray neutrino transport and coupled neighboring rays in 2D hydrodynamic simulations.

Studying the matter GW signal alone is worthwhile. Although the neutrino GW strain amplitudes can be as large or even larger than the contribution by matter (Burrows & Hayes 1996; Müller & Janka 1997; Müller et al. 2004; Marek et al. 2009), the typical frequencies,  $f$ , of the neutrino GW signal ( $\sim 10$  Hz or less) are typically much lower than the frequencies of the matter signal ( $\gtrsim 100$  Hz). Consequently, the GW power emitted, which is proportional to  $f^2$ , can be much higher for the matter GW signal. Furthermore, although future GW detectors (e.g., Advanced LIGO) will have improved sensitivity at low frequencies, current detectors have response curves that are not sensitive to the lower frequencies of the neutrino GW signal.

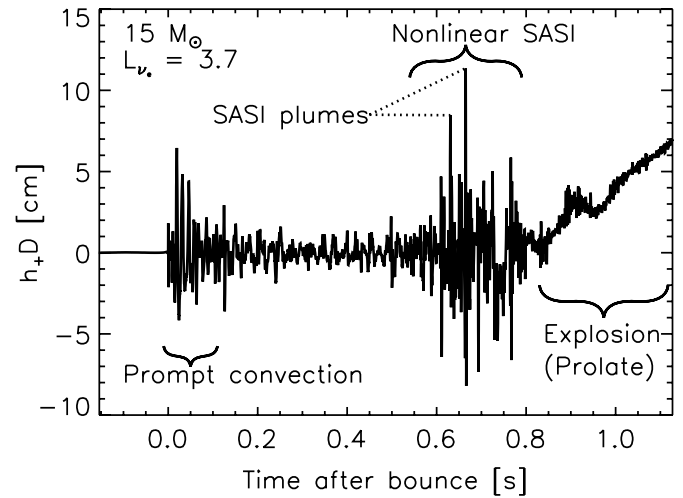


**Figure 2.** Sample of GW strain ( $h_+$ ) times the distance,  $D$ , vs. time after bounce. This signal was extracted from a simulation using a  $15 M_{\odot}$  progenitor model (Woosley & Heger 2007) and an electron-type neutrino luminosity of  $L_{\nu_e} = 3.7 \times 10^{52}$  erg  $s^{-1}$ . Prompt convection, from a negative entropy gradient left by the stalling shock, is the first distinctive feature in the GW signal from 0 to  $\sim 50$  ms after bounce. From  $\sim 50$  ms to  $\sim 550$  ms past bounce, the signal is dominated by PNS and postshock convection. Afterward and until the onset of explosion ( $\sim 800$  ms), strong nonlinear SASI motions dominate the signal. The most distinctive features are spikes that correlate with dense and narrow down-flowing plumes striking the “PNS” surface ( $\sim 50$  km). Around  $\sim 800$  ms, the model starts to explode. In this simulation, the GW signal during explosion is marked by a significant decrease in nonlinear SASI characteristics. The aspherical (predominantly prolate) explosion manifests in a monotonic rise in  $h_+D$  that is similar to the “memory” signature of asymmetric neutrino emission.

### 3.2. Signatures in the GW Strain

In Figure 1, we plot the GW strain (Equation (13)) times the distance to a 10 kpc source,  $h_+D$ , versus time after bounce for all simulations. Though there is some diversity in amplitude and timescale among these GW strains, there are several recurring features that exhibit systematic trends with mass and neutrino luminosity. We illustrate these features in Figure 2 with the GW strain of the simulation using the  $15 M_{\odot}$  progenitor and  $L_{\nu_e} = 3.7 \times 10^{52}$  erg  $s^{-1}$ . Before bounce, spherical collapse results in zero GW strain. Just after bounce the prompt shock loses energy and stalls, leaving a negative entropy gradient that is unstable to convection. Because the speeds of this prompt convection are larger than those of steady-state postshock or PNS convection afterward, the GW strain amplitude rises to  $h_+D \sim 5$  cm during prompt convection and settles down to  $\sim 1$  cm roughly 50 ms later, which is consistent with the results of Ott (2009b) and Marek et al. (2009). Later in this section, we show that during both phases, convective motions in postshock convection above the neutrinosphere and PNS convection below it contribute to the GW strain. Since nonlinear SASI oscillation amplitudes increase around 550 ms past bounce, the GW signal strengthens from  $h_+D \sim 1$  to 10 cm and is punctuated by spikes that are coincident in time with narrow plumes striking the PNS “surface” (at  $\sim 50$  km). Marek et al. (2009) also noted this correlation.

The final feature after  $\sim 800$  ms is associated with explosion. The signatures of explosion are twofold. First, during explosion, postshock convection and the SASI subside in strength and the higher frequency ( $\sim 300$ – $400$  Hz) oscillations in  $h_+D$  diminish. Second, global asymmetries in mass ejection result in long-term and large deviations of the GW strain. In Figure 2, a monotonic rise of  $h_+D$  to nonzero, specifically positive, values corresponds

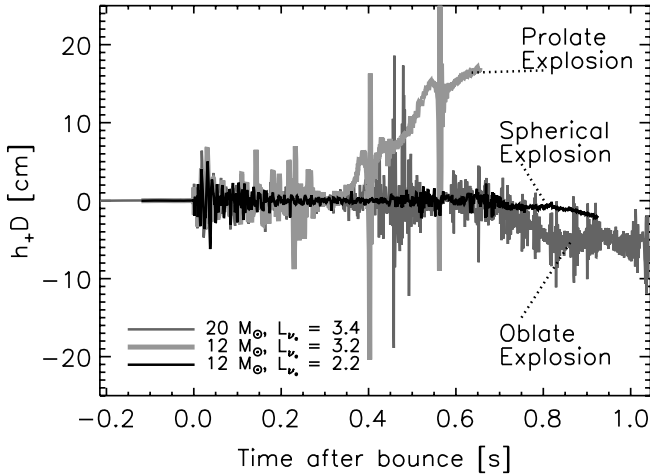


**Figure 3.** Plots of  $h_+D$  vs. time after bounce for three models showing the effect of global asymmetries in explosion. The general shapes of the explosions are prolate ( $M = 12 M_\odot$ ,  $L_{\nu_e} = 3.2 \times 10^{52} \text{ erg s}^{-1}$ , and thick light-gray line), spherical ( $M = 12 M_\odot$ ,  $L_{\nu_e} = 2.2 \times 10^{52} \text{ erg s}^{-1}$ , and thin black line), and oblate ( $M = 20 M_\odot$ ,  $L_{\nu_e} = 3.4 \times 10^{52} \text{ erg s}^{-1}$ , and thin gray line), and correspond to positive, zero, and negative “memory,” respectively. See Figure 4 for color maps of the entropy distribution during explosion for the same models.

to a prolate explosion in this simulation. This is similar to the “memory” in the GW signal of asymmetric neutrino emission (Burrows & Hayes 1996; Müller & Janka 1997). When the explosion is spherical, the strain drops to zero and remains there, and when it is oblate, the strain maintains negative values. Examples of  $h_+D$  curves showing prolate, oblate, and spherical explosions are shown in Figure 3. The simulation using a  $20 M_\odot$  progenitor and  $L_{\nu_e} = 3.4 \times 10^{52} \text{ erg s}^{-1}$  (gray line) exploded with an oblate structure, the simulation with  $M = 12 M_\odot$  and  $L_{\nu_e} = 3.2 \times 10^{52} \text{ erg s}^{-1}$  (light gray line) has a prolate explosion, and the simulation with  $M = 12 M_\odot$  and  $L_{\nu_e} = 2.2 \times 10^{52} \text{ erg s}^{-1}$  explodes almost spherically.

Figure 4 shows snapshots of the entropy (in units of  $k_B/\text{baryon}$ ) distribution during explosion for the three models highlighted in Figure 3. Lighter shades (warmer colors in the online version) represent higher entropies, while darker shades (cooler colors in the online version) represent lower entropies. The general shapes of the matter interior to the shocks is oblate ( $M = 20 M_\odot$  and  $L_{\nu_e} = 3.4 \times 10^{52} \text{ erg s}^{-1}$ ), prolate ( $M = 12 M_\odot$  and  $L_{\nu_e} = 3.2 \times 10^{52} \text{ erg s}^{-1}$ ), and spherical ( $M = 12 M_\odot$ ,  $L_{\nu_e} = 2.2 \times 10^{52} \text{ erg s}^{-1}$ ; and thin black line). We emphasize that the GW signal is sensitive to  $\ell = 2$  accelerations of matter and is somewhat blind to differences in composition or higher order asymmetries. Therefore, even though the GW signal may indicate that the explosion is in general “spherical,” “oblate,” or “prolate,” the entropy (hence temperature and composition) distributions may not be.

In Figures 5 and 6, we localize the source of GW emission. Figure 5 shows the spatial distribution of

$$\left| \frac{d}{dt} \left[ r^3 \rho \left( P_2(\cos \theta) v_r + \frac{1}{2} \frac{\partial}{\partial \theta} P_2(\cos \theta) v_\theta \right) \right] \right|, \quad (21)$$

which is the time derivative of the integrand of Equation (12) and determines the GW strain (Equation (13)). As in Figure 2, these results are for the  $15 M_\odot$  progenitor and  $L_{\nu_e} = 3.7 \times 10^{52} \text{ erg s}^{-1}$ . Lighter shades (brighter colors in the online version) correspond to a larger contribution to the GW strain integral. The left panel is at 615 ms past bounce, and represents the phase with a stalled shock ( $\sim 250 \text{ km}$ ) and vigorous postshock-convection/SASI motions. This is our first indication that motions below the gain radius ( $\sim 100 \text{ km}$ ), in particular deceleration of plumes and PNS convection, are the strongest sources of GWs before explosion.

The right panel is at 1060 ms past bounce and shows that accelerations at an aspherical shock ( $\sim 4000 \text{ km}$  at this time) are responsible for the “memory” signature at late times. Using the appropriate shock velocities and asymmetries and postshock

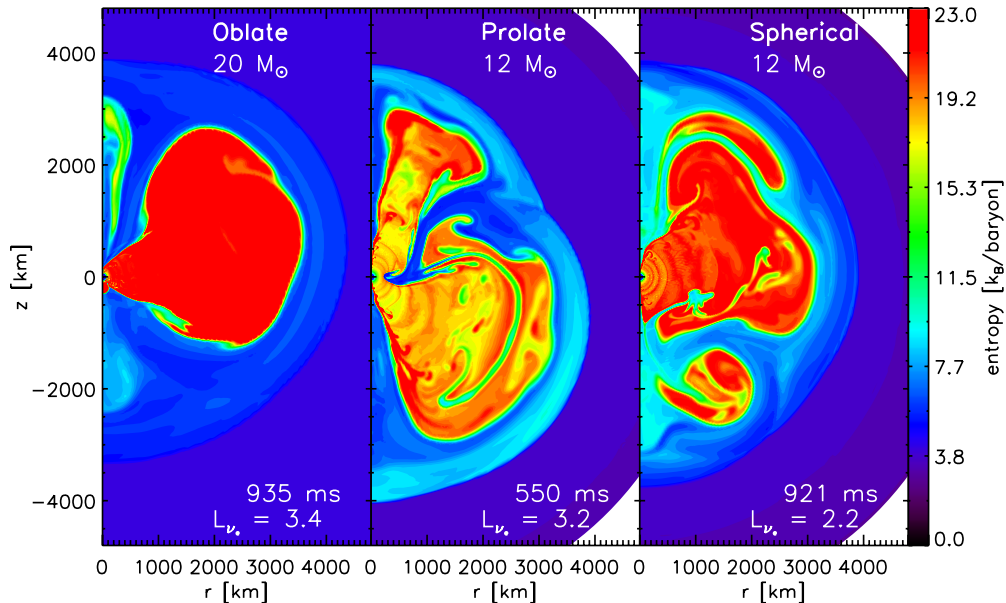


**Figure 4.** Snapshots of the entropy ( $k_B/\text{baryon}$ ) distribution during explosion for the three models highlighted in Figure 3. Lighter shades (warmer colors in the online version) represent higher entropies, while darker shades (cooler colors in the online version) shades represent lower entropies. The global asymmetry of the matter interior to the shocks is oblate ( $M = 20 M_\odot$  and  $L_{\nu_e} = 3.4 \times 10^{52} \text{ erg s}^{-1}$ ), prolate ( $M = 12 M_\odot$  and  $L_{\nu_e} = 3.2 \times 10^{52} \text{ erg s}^{-1}$ ), and spherical ( $M = 12 M_\odot$ ,  $L_{\nu_e} = 2.2 \times 10^{52} \text{ erg s}^{-1}$ ). Even though the GW signal may indicate that the explosion is in general “spherical,” “oblate,” or “spherical,” the entropy (hence temperature and composition) distributions may show higher order structure.

(A color version of this figure is available in the online journal.)

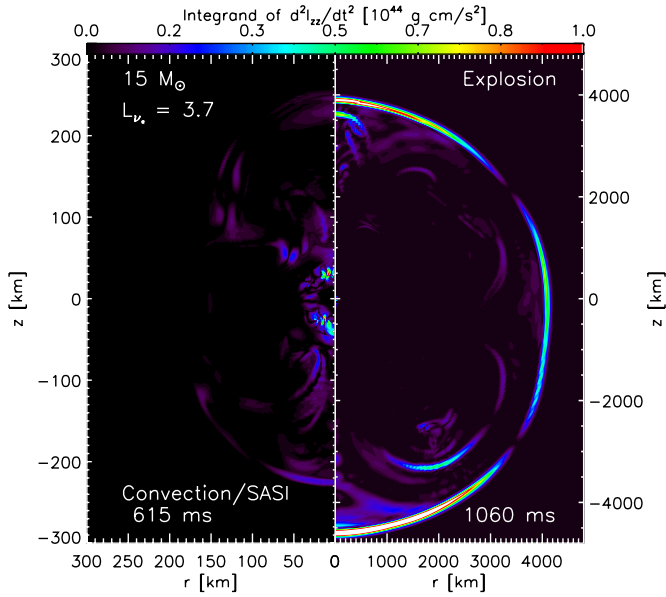


**Figure 5.** Gray-scale (color in the online version) map of the integrand that leads to the GW signal (see Equations (12), (13), and (21)). Lighter shades (brighter colors in the online version) correspond to higher values. The results are for the  $15 M_{\odot}$  progenitor and  $L_{\nu_e} = 3.7 \times 10^{52}$  erg  $s^{-1}$ . The left panel represents the stalled-shock phase during vigorous postshock-convection/SASI motions. During this phase, the signal originates predominantly from PNS convection and the deceleration of plumes below the gain radius ( $\sim 100$  km). The right panel shows that the “memory” signal during explosion is a result of acceleration at an asymmetric shock.

(A color version of this figure is available in the online journal.)

densities and velocities in Equations (12) and (13), we obtain the correct order of magnitude for the memory signal. However, during explosion a high entropy wind emerges that encounters the swept-up material of the primary shock and produces secondary shocks. We find that these secondary shocks and their asymmetric structure can add a non-trivial contribution to the “memory” signal. The strength of these winds is a strong function of the neutrino luminosity (Qian & Woosley 1996; Thompson et al. 2001). Since we employ a constant neutrino luminosity, an accurate characterization of the late-time “memory” (such as saturation) are beyond the scope of this paper.

Figure 6 quantifies the sources of GW radiation and their spatial distribution as a function of radius. The model shown is the same as in Figures 2 and 5. For reference, the entire GW signal is shown in both panels (solid-black line). The signals originating from  $>50$  km (orange, online version) and  $<50$  km (blue, online version) are shown in the top panel. Below 50 km, PNS convection dominates the motions, and above this radius postshock convection and the SASI dominate. As expected, most of the signal associated with prompt convection originates in the outer convective zone, though motions below 50 km and presumably from PNS convection account for a fair fraction ( $\sim 20\%$ ). Afterward, the contributions to the GW amplitude from below and above 50 km are comparable. This suggests that motions associated with both PNS convection and the postshock-convection/SASI region contribute significantly to the GW signal. The “memory” signature of the GW strain during explosion clearly originates from the outer (exploding) regions. Interestingly, once the model explodes, and the nonlinear postshock-convection/SASI motions subside, the GW signal from below 50 km diminishes as well, though PNS convective motions do not.

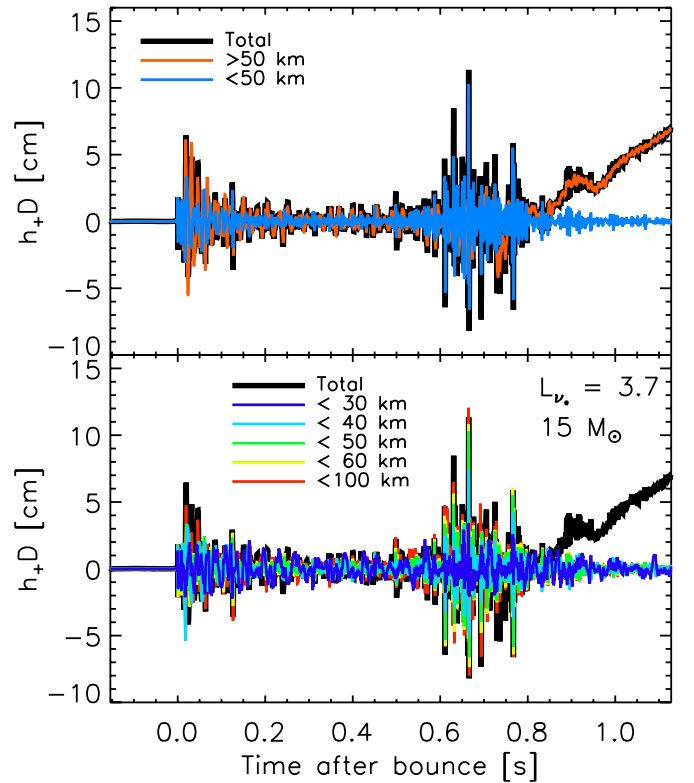


**Figure 6.** GW waveforms,  $h_+D$  vs. time, showing the contributions of PNS convection and the SASI. The model shown is the same as in Figure 2. For reference, the entire GW signal is shown in both panels (solid-black line). The signal originating from  $>50$  km (orange, online version) and  $<50$  km (blue, online version) is shown in the top panel. This radius is roughly the division between nonlinear SASI motions and PNS convection motions. Most, but not all, of the signal associated with prompt convection originates in the outer convective zone. There is a non-negligible contribution from the PNS. The monotonic rise in the GW strain during explosion clearly originates from the outer (exploding) regions. Even though the region for the convection/SASI and its nonlinear motions are above 50 km, these motions influence the PNS convective motions below 50 km. It is telling that once the model explodes, and the nonlinear SASI motions subside but the PNS convection does not, the GW signal from below 50 km diminishes as well. The bottom panel shows the GW signal from five regions, each with different outer radii (30, 40, 50, 60, and 100 km). The strengthening of the GW signal associated with the SASI is apparent for all, suggesting that the influence of the SASI diminishes only gradually with depth.

(A color version of this figure is available in the online journal.)

To further understand the origin of GW emission, the bottom panel of Figure 6 refines the spatial origin of the GW emission into five regions. We plot the GW strain from five overlapping regions, and each extends from the center to different outer radii (30, 40, 50, 60, and 100 km). PNS convection extends from  $\sim 20$  to  $\sim 40$  km and the gain radius is  $\sim 100$  km. However, as we explain in section Section 3.4, the turbulent motions of postshock convection/SASI penetrate below the gain radius to radii of  $\sim 60$  km during the most vigorous phases. Therefore, the partial GW signals with outer radii of 30 and 40 km contain signals only due to PNS convection; 50 km encompasses PNS convection and gravity waves that are excited by the overlying convection/SASI; 60 km encompasses PNS convection, gravity waves, and the deepest penetration of the convection/SASI plumes (see Section 3.4); and 100 km encompasses all of these contributions and the gain radius. First, we note that extending the outer radius from 60 to 100 km, the gain radius, adds very little signal during the most vigorous postshock-convection/SASI phase from 550 to 800 ms past bounce. Therefore, the

most relevant motions are those at  $\sim 60$  km and below, which include the postshock-convection/SASI plume decelerations, excited gravity waves, and PNS convection. Furthermore, the strength of the GW signal from all radii increases and decreases in synchrony with the vigor of postshock-convection/SASI motions, which are restricted to radii above  $\sim 50$  km. This suggests that the influence of the convection/SASI diminishes only gradually with depth. Even though the mechanism for convection/SASI and their nonlinear motions are above 50 km, they influence PNS convective motions below 50 km, which results in GW emission whose vigor is ultimately due to the postshock-convection/SASI motions.

Hence, we conclude that features of the SASI and postshock convection, in particular the plumes striking the PNS “surface,” are ultimately responsible for the strong GW signal from  $\sim 550$  ms until explosion at  $\sim 800$  ms after bounce. Some of the signal comes from the accelerations at this interface. The rest comes from gravity waves and motions within the PNS ( $< 50$  km) that are excited by the plumes striking this layer. Whether these motions are excited  $g$ -waves, enhanced PNS convection, or a combination of both is difficult to distinguish in our simulations. A focused investigation on this aspect is warranted.

Müller et al. (2004) conclude that the GW signal from PNS convection is a few factors smaller in amplitude than the GWs from postshock convection. At first sight, this conclusion appears at odds with our results that the signals above and below 50 km are roughly equal. However, to calculate the GW signal from PNS convection, Müller et al. (2004) used results from a simulation that extended out to only 60 km (Keil et al. 1996), which ignores any influence that postshock-convective or SASI motions have on PNS convection. This is consistent with the GW signal we obtain after explosion, when postshock convection and SASI go away, but PNS convection remains. These results emphasize the importance of calculating PNS convection in the full context of core-collapse dynamics.

We now return to Figure 1 and analyze the trends with progenitor mass and  $L_{\nu_e}$ . Each panel represents a single progenitor model and the curves are labeled by  $L_{\nu_e}$ . The accretion rates (in  $M_{\odot} \text{ s}^{-1}$ ) at the stalled shock of non-exploding models are shown for comparison. The prominent features described in Figure 2 are apparent in all models, except the run using  $M = 40 M_{\odot}$  and  $L_{\nu_e} = 6.0 \times 10^{52} \text{ erg s}^{-1}$  that does not explode and manifests the larger amplitudes associated with the nonlinear SASI at much later times. Otherwise, lower luminosity simulations take longer to develop the nonlinear SASI GW signal and explode at later times, but all runs seem to saturate at roughly similar amplitudes. This is consistent with the results of Murphy & Burrows (2008b), in which they note that lower luminosity runs take longer to reach saturated shock oscillations, but that the saturated amplitudes are similar for the different neutrino luminosities. Similarly, Kotake et al. (2009) conclude that the GW amplitudes are independent of neutrino luminosity. Finally, we note that the significant drop in accretion rate in simulations using the  $20 M_{\odot}$  progenitor, instigates strong nonlinear SASI motions and associated GW signatures. This might suggest using GWs as a diagnostic for the location of shell burning or compositional interfaces. However, very few of the other simulations show such a convincing correlation.

The neutrino luminosities required to explode the  $40 M_{\odot}$  progenitor model are much larger than simulations obtained that consistently calculate neutrino transport (Dessart et al. 2006; Ott et al. 2008; Marek & Janka 2009). Therefore, if other

mechanisms fail to explode higher mass stars, we suspect that the simulation using  $L_{\nu_e} = 6 \times 10^{52} \text{ erg s}^{-1}$ , which does not explode by the neutrino mechanism, gives an upper limit on the most likely GW emission strength for massive progenitors that collapse to form black holes without explosion. Taken at face value, the low convective and SASI motions of this model imply that, in the absence of rapid rotation, the GW power emitted by the most massive progenitors that form black holes could be quite low.

### 3.3. GW Energy Spectra and Detection

If rotation rates are low and PNS core  $g$ -modes are weak, then postshock-convection/SASI motions are the most probable source of GWs. In this scenario, the GW emission of Galactic CCSNe ( $\sim 10$  kpc) is probably too weak to detect the GW strain waveform directly as a time series. Instead, GW observers will search for excess spectral power above the detector noise in time–frequency maps (e.g., Abbott et al. 2009). The energy spectra versus frequency for all simulations is plotted in Figure 7 assuming a distance to the source,  $D$ , of 10 kpc. Rather than showing  $dE_{\text{GW}}/df$ , we plot  $h_{\text{char}}$  (Equation (17)), which is proportional to  $\sqrt{dE_{\text{GW}}/df}$ . As in Figure 1, each panel shows the spectra from simulations for the same progenitor model, and within each panel the spectra are color-coded and labeled by  $L_{\nu_e}$ . For reference, the noise thresholds for Initial LIGO (solid black line, Gustafson et al. 1999), Enhanced LIGO (dot-dashed-black line; R. Adhikari 2009, private communication), and Advanced LIGO (burst mode, dashed-black line; D. Shoemaker 2006, private communication) are included.

Characteristically, the spectra show broad peaks with maximum power at  $\sim 300$  to  $\sim 400$  Hz. The lower and higher frequencies correspond to lower and higher progenitors masses, respectively. Later in this section and Section 3.4, in analyzing the spectra as a function of postbounce time, we show in Figure 8 that simulations with lower  $L_{\nu_e}$  explode later and obtain higher frequencies at later times. However, the spectra in Figure 7, which are calculated using the entire time sequence, do not clearly show such a correlation. The spectra associated with 12, 15, and  $20 M_{\odot}$  progenitors show a second, weaker peak at  $\sim 100$  Hz that we associate with prompt convection. Generally, all spectra are only marginally above or just below the design noise threshold for Initial LIGO. On the other hand, all simulations have power above the design noise threshold for Enhanced and Advanced LIGOs, with maximum spectral signal-to-noise ratios of  $\sim 5$  and  $\sim 10$ – $20$ , respectively.

Characteristic GW amplitudes, frequencies, optimal theoretical single-detector signal-to-noise ratios, and energies for all simulations presented in this paper are listed in Table 1. The first two columns identify the progenitor mass and neutrino luminosity of the simulation. Following are the maximum amplitude of the GW strain ( $|h_{+, \text{rms}}|$ ), the signal-to-noise ratios with respect to the Initial, Enhanced, and Advanced LIGO sensitivity curves ( $S/N_{\text{LIGO}}$ ,  $S/N_{\text{eLIGO}}$ , and  $S/N_{\text{advLIGO}}$ ). We also provide values for the emitted GW energy ( $E_{\text{GW}}$ ) and  $h_{\text{char}}$  (Equation (17)) for the maxima of the characteristic strain spectra and the frequencies  $f_{\text{char, max}}$  at which they are located. The values in this table do not present clean, monotonic trends with progenitor mass or neutrino luminosity. However, we note some general trends. More massive progenitors tend to produce higher frequencies.<sup>10</sup>

<sup>10</sup> Burrows et al. (2007c) show in Table 1 of their paper a similar trend in that higher progenitor masses produce higher shock-oscillation frequencies, though at much smaller values.

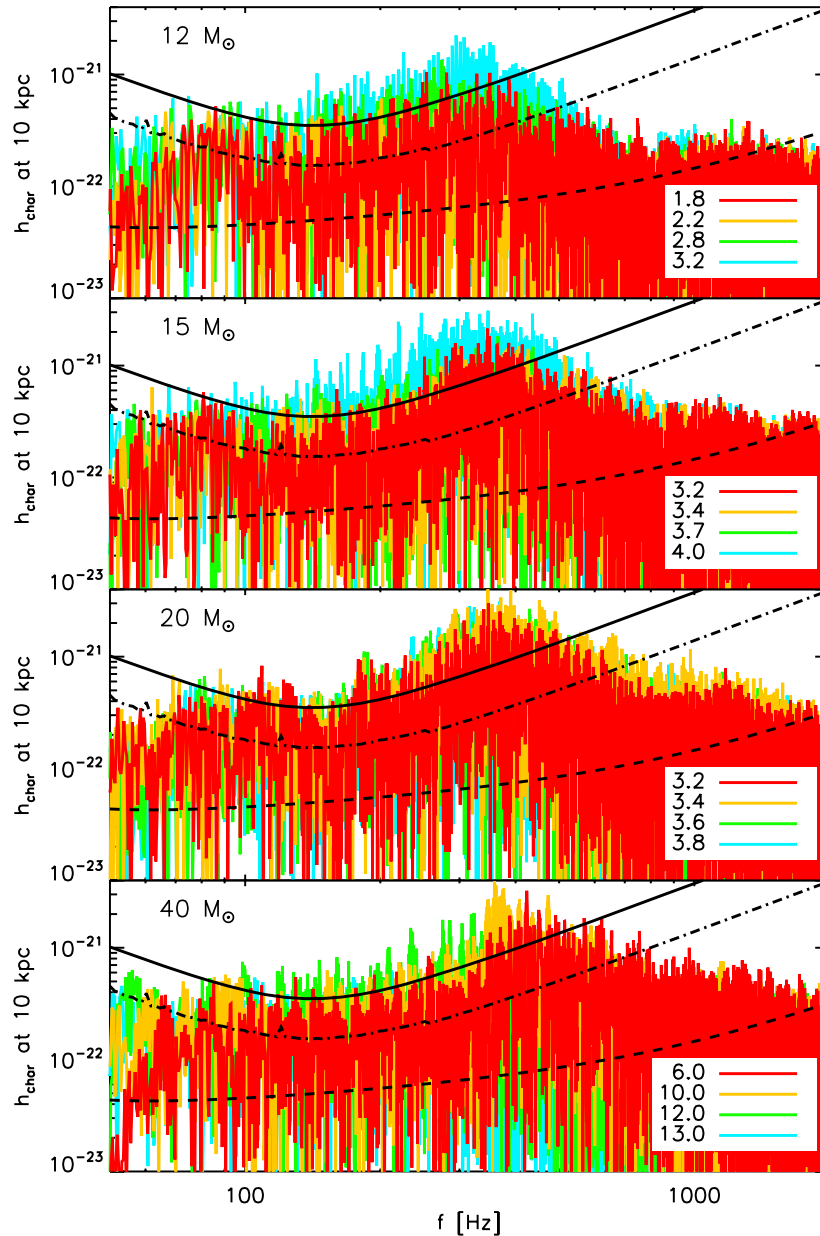


**Figure 7.**  $h_{\text{char}}$  (Equation (17)) vs. frequency for the suite of simulations presented in this paper. The spectra show broad peaks and some dependence upon the progenitor mass:  $\sim 300$  Hz for  $12 M_{\odot}$  and  $\sim 400$  Hz for  $40 M_{\odot}$ . The power of the spectra show only a slight increase (if at all) with neutrino luminosity. For comparison, the approximate noise thresholds for Initial LIGO (solid-black curve), Enhanced LIGO (dot-dashed-black curve), and Advanced LIGO (dashed-black curve) are plotted. (A color version of this figure is available in the online journal.)

On the other hand, for a given progenitor model, higher neutrino luminosities give lower frequencies. In Section 3.4, we explain that the characteristic frequency of GWs is connected with the buoyancy frequency in the postshock region, which is higher for more massive progenitors, increases with time, and is largely independent of neutrino luminosity. This explains the first correlation with progenitor mass, but to explain the anti-correlation with neutrino luminosity, we note that the higher luminosity simulations explode earlier when the buoyancy frequency is lower.

In general, the typical GW strain for a source at 10 kpc is a few times  $10^{-22}$  to  $10^{-21}$ , and typical values of  $E_{\text{GW}}$  range from a few times  $10^{-11}$  to a few times  $10^{-10} M_{\odot} c^2$ . Kotake et al. (2009) conclude that the stochastic properties of the SASI preclude any relationship between the neutrino luminosity and the GW amplitude. While there appears to be no trends, we note several

competing dependencies on neutrino luminosity that result in a non-monotonic and complicated relationship. In Section 3.4, we connect the GW amplitude to the speed of plumes,  $v_p$ , at the base of the SASI region. In addition, we note that although lower luminosity simulations take longer to saturate the SASI motions, the saturation value eventually achieved is similar for all runs. Since most of the GW power is emitted during the phase of strongest postshock-convection/SASI motions, the total energy emitted is determined by the duration of this phase, which starts earlier for the higher neutrino luminosity, but also ends much earlier at the higher luminosities, so that the total duration of the stronger SASI phase, and therefore,  $E_{\text{GW}}$  is a non-monotonic function of neutrino luminosity.

Focusing on the energy spectrum for an entire GW strain data set is most appropriate when the signal is regular in both amplitude and frequency. However, Figures 1 and 2

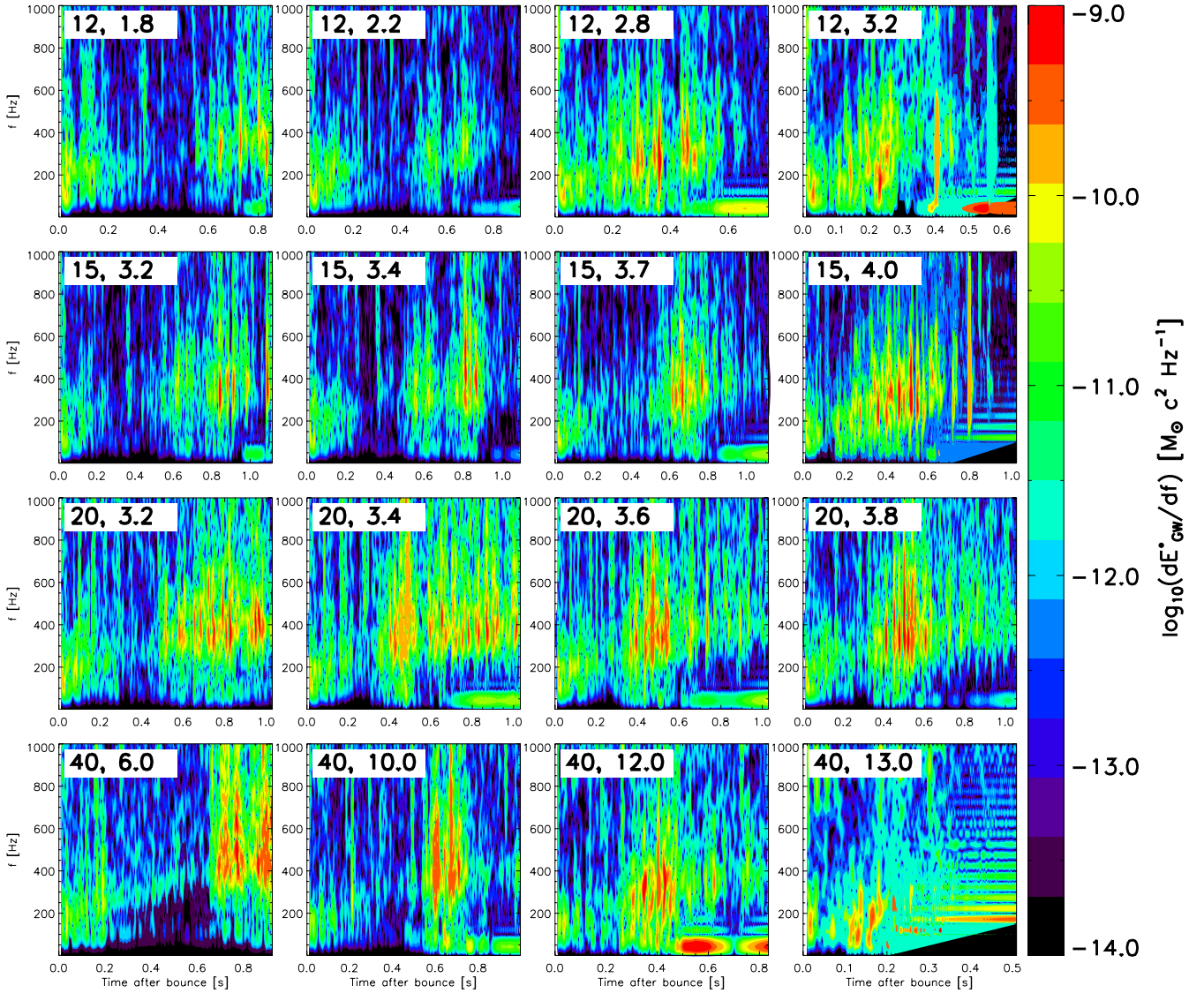


**Figure 8.** Spectrograms of the GW signals showing  $dE_{\text{GW}}^*/df$  as a function of frequency (vertical axes) and time (horizontal axes) after bounce for the entire set of simulations presented in this paper. Bursts of power are associated with prompt convection and the SASI. Frequency at peak power increases from  $\sim 100$  Hz to  $\sim 300$ – $400$  Hz, depending upon the explosion time and progenitor used. We show in Section 3.4 that this frequency and the trend to higher frequencies is a consequence of the core structure. During explosion, GW power transitions to lower frequencies ( $\sim 10$ s of Hz).

(A color version of this figure is available in the online journal.)

show that the amplitude and frequency change substantially in these simulations. In this case, a time–frequency analysis, or spectrogram, is more appropriate (see Section 3.1). To obtain energy spectra versus time we take the Fourier transform of the GW strain convolved with a Hann window function with width  $\sim 20$  ms and sample the time domain,  $\tau$  in Equation (18), at intervals of 2 ms. In Figure 8, we show color maps of  $dE_{\text{GW}}^*/df$  (Equation (20)) versus frequency and time. The warmer colors in Figure 8 reflect higher power, and vice versa for cooler colors. In general, simulations that explode later (i.e., with higher mass progenitors and/or lower neutrino luminosities) have GW power at higher frequencies. During explosion, the frequency at peak power drops to 10s of Hz, owing to asymmetric mass ejection.

Unlike in the spectra, which are calculated using the entire time domain (Figure 7), prompt convection, nonlinear SASI, SASI plumes, and explosion are quite apparent in these time–frequency plots. Figure 9 labels these features in the spectrogram for the simulation using  $M = 15 M_{\odot}$  and  $L_{\nu_e} = 3.7 \times 10^{52}$  erg s $^{-1}$ . The three features showing the largest

power are prompt convection just after bounce, nonlinear SASI motions, and explosion. Though the power declines between prompt convection and the start of the nonlinear SASI, the frequency at peak power increases monotonically from  $\sim 100$  Hz at bounce to  $\sim 300$ – $400$  Hz just before explosion. In the next section, we propose that the characteristic timescale for the deceleration of plumes striking the PNS “surface” determines the GW peak frequencies. The solid black line in Figure 9 shows our analytic estimate for this characteristic frequency,  $f_p$ , and that it agrees with the frequency and time evolution of the GW signal from simulation.

#### 3.4. Source of GWs and a Theory for Their Characteristic Frequencies and Amplitudes

Figure 6 shows that motions associated with the broad region, which includes PNS convection, postshock convection, and the SASI, contribute to the overall GW signal. Marek et al. (2009) come to a similar conclusion. However, in Sections 3.2 and 3.3, we noted that the strength of the GW signal waxes and wanes as

**Table 1**  
Quantitative Summary of GW Characteristics<sup>a</sup>

Mass <sup>b</sup>	$L_{\nu_e}$ <sup>c</sup>	$ h_{+,max} $ <sup>d</sup>	S/N <sub>LIGO</sub> <sup>e</sup>	S/N <sub>eLIGO</sub> <sup>f</sup>	S/N <sub>advLIGO</sub> <sup>g</sup>	$h_{char,max}$ <sup>h</sup>	$f_{char,max}$ <sup>i</sup>	$E_{GW}$ <sup>j</sup>
12	1.8	0.27	0.8	2.0	7.9	1.04	253	6.1
12	2.2	0.20	0.7	1.7	6.7	0.61	200	3.5
12	2.8	0.46	1.2	2.7	10.8	1.35	273	8.5
12	3.2	1.13	1.6	4.0	15.7	2.23	294	20.4
15	3.2	0.37	1.1	2.6	11.4	2.14	345	17.5
15	3.4	0.40	1.0	2.4	10.2	1.49	406	14.4
15	3.7	0.37	1.1	2.8	11.5	1.83	365	12.8
15	4.0	1.53	2.1	5.3	21.2	3.10	347	46.1
20	3.2	0.32	1.4	3.4	14.5	3.00	348	29.5
20	3.4	0.70	1.8	4.5	19.5	4.68	347	57.8
20	3.6	0.56	1.5	3.9	16.1	2.67	429	34.5
20	3.8	0.48	1.5	3.8	15.7	3.14	369	33.8
40	6.0	0.33	1.0	2.6	12.2	3.23	423	36.2
40	10.0	0.68	1.4	3.6	17.3	3.93	359	47.1
40	12.0	0.82	1.4	3.4	14.0	2.04	323	16.6
40	13.0	4.53	0.8	1.8	9.4	1.08	1 <sup>k</sup>	4.1

**Notes.**

<sup>a</sup> This table lists the integrated GW characteristics of the 2D simulations. These simulations represent a two-dimensional parameterization that investigates the dependence of GW emission on progenitor mass (Column 1) and neutrino luminosity (Column 2).

<sup>b</sup> Progenitor model ( $M_{\odot}$ ).

<sup>c</sup> Neutrino luminosity ( $10^{52}$  erg s<sup>-1</sup>).

<sup>d</sup> Maximum GW strain ( $10^{-21}$  at 10 kpc).

<sup>e</sup> Optimal theoretical single-detector signal-to-noise ratio using the Initial LIGO sensitivity curve (Gustafson et al. 1999).

<sup>f</sup> Optimal theoretical signal-to-noise ratio using the Enhanced LIGO sensitivity curve (R. Adhikari 2009, private communication).

<sup>g</sup> Optimal theoretical single-detector signal-to-noise ratio using the burst-mode Advanced LIGO sensitivity curve (D. Shoemaker 2006, private communication).

<sup>h</sup> Maximum of the characteristic strain spectrum defined in Equation (17) ( $10^{-21}$  at 10 kpc).

<sup>i</sup> Frequency location of  $h_{char,max}$  (Hz).

<sup>j</sup> GW energy emitted ( $10^{-11} M_{\odot} c^2$ ).

<sup>k</sup> Because this simulation explodes early and with large asymmetry, the low-frequency “memory” signature in the GW strain dominates the energy spectrum.

the vigor of postshock-convection and SASI motions rises and falls. Moreover, spikes in the GW strain often correlate in time with downdrafts (plumes) striking the PNS “surface” (also noted by Marek et al. 2009). Hence, we argue that the strength and characteristic frequencies of the GW emission are determined predominantly by the deceleration of the plumes striking the PNS “surface.”

In other contexts, the “surface” of the PNS is defined as the position of the neutrinosphere, the location of a steepening density gradient, or the narrow region over which the average radial velocity of the accreting matter approaches zero. These definitions roughly coincide in space and are in fact intimately related, but they neither explain nor quantify the strong decelerations of the downdrafts in an otherwise continuous medium. We note, however, that buoyancy forces and their radial profile at the boundary between convective and stably stratified regions explain the deceleration of the plumes and, hence, the GW amplitudes and frequencies. We, therefore, define the PNS “surface” as the region where the negatively buoyant downdrafts become positively buoyant and reverse their downward motions.

An important quantity in analyzing convection and buoyancy is the square of the Brunt–Väisälä (or buoyancy) frequency

$$N^2 = \left( \frac{GM_r}{r^3} \right) \left( \frac{1}{\Gamma_1} \frac{d \ln P}{d \ln r} - \frac{d \ln \rho}{d \ln r} \right), \quad (22)$$

where  $M_r$  is the mass interior to the radius,  $r$ , and the thermodynamic derivative,  $\Gamma_1 = (\partial \ln P / \partial \ln \rho)_S$ , is evaluated at constant entropy,  $S$ . In the local dispersion relation for waves, this corresponds to the characteristic frequency associated with gravity

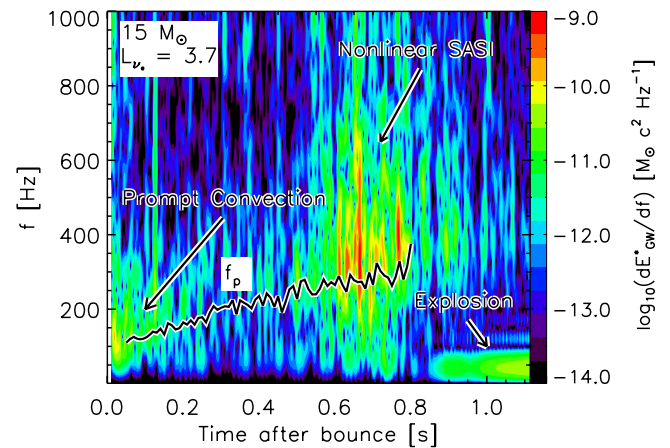


**Figure 9.** Spectrogram,  $dE_{GW}^*/df$ , and characteristic plume deceleration frequency,  $f_p$ , vs. time after bounce for the simulation using the  $15 M_{\odot}$  progenitor and  $L_{\nu_e} = 3.7 \times 10^{52}$  erg s<sup>-1</sup>. Similar to Figure 2, the three features showing the largest power are prompt convection just after bounce, nonlinear SASI plumes/motions, and explosion. Unlike in the GW strain, the specific morphology of the explosion, other than it is asymmetric, is not discernible in the spectrogram. From bounce until explosion, the frequency at peak power agrees with  $f_p$ . This strong correlation persists whether prompt convection, convection, or the SASI are the dominant hydrodynamic processes and implies that the plume’s buoyant deceleration determines the characteristic GW frequency.

(A color version of this figure is available in the online journal.)

waves (not to be confused with GWs), whose dominant restoring force is buoyancy, which sets the frequency scale. Alternatively,  $N^2 < 0$  indicates linear instability and is in fact the Ledoux (and Rayleigh–Taylor) condition for convection. Naively, one

might expect the radius where  $N^2$  changes sign from negative to positive to mark the lower boundary of the convection zone. However, the Ledoux condition is derived from a linear analysis and ignores important nonlinear effects. In practice, convective plumes have momentum when they reach this boundary and penetrate beyond the Ledoux condition boundaries. This is called overshoot and has a long history and many proposed prescriptions, though many of these are either inappropriate for the dynamics in core-collapse SNe or lack adequate physical motivation, resulting in a free parameter (see Meakin & Arnett 2007b; Arnett et al. 2009; and the references therein). For this paper, we adopt an analysis based upon buoyancy and the bulk Richardson number (Meakin & Arnett 2007b), which is physically motivated and contains no free parameters.

Beyond the boundaries defined by the Ledoux condition,  $N^2$  is positive and, therefore, coherent plumes that penetrate this boundary experience a buoyancy force back toward the central regions of convection. In this context, the buoyancy acceleration,  $b(r)$ , felt by a Lagrangian mass element displaced from  $r_i$  to  $r$  is related to the buoyancy frequency by

$$b(r) = \int_r^{r_i} N^2(r) dr. \quad (23)$$

For plumes approaching the lower boundary of postshock convection, the magnitude of the integrand is largest where  $N^2 > 0$ . Therefore, we take as  $r_i$  the lower Ledoux condition boundary. With a plume velocity in the radial direction,  $v_p$ , at  $r_i$  as initial conditions and Equation (23) as the position dependent acceleration, we integrate the plume's equation of motion to determine the depth of penetration,  $D_p$ . Because the sources of GWs are time-changing quadrupole motions, the inverse of the characteristic time of the buoyancy impulse for each plume should correspond roughly to the peak frequencies in the GW spectra and spectrograms (Figures 7 and 8). This timescale,  $t_p$ , is defined as the half-width at half-maximum (HWHM) of the buoyancy acceleration pulse and the associated frequency is  $f_p = 1/(2\pi t_p)$ .<sup>11</sup> It is this definition of  $f_p$  for which we give quantitative results in this paper.

Using the bulk Richardson number, a dimensionless measure of the boundary layer stiffness, we obtain an analytic description of  $f_p$  that is independent of, and corroborates, our method for calculating  $f_p$ . There is a long tradition of using this dimensionless parameter in atmospheric sciences to accurately describe the boundary layer in atmospheric convection (Fernando 1991; Fernando & Hunt 1997; Bretherton et al. 1999; Stevens 2002). More recently Meakin & Arnett (2007b) have successfully used similar arguments to describe the boundaries of convection in stellar evolution. The bulk Richardson number is

$$R_b = \frac{\Delta b D_p}{v_p^2}, \quad (24)$$

where  $\Delta b$  is the change in buoyancy acceleration across the boundary,  $D_p$  is a length scale such as the penetration depth, and  $v_p^2$  is the typical velocity of the plume. This is not to be confused with the *gradient* Richardson number,  $R_g$ , which is derived from a linear analysis and is a condition for shear instabilities in a stratified medium. While  $R_g = 1/4$  is the derived value that separates stability from instability in a linear

analysis,  $R_b$  is a rough measure of the stiffness of a stable layer next to a convective layer in nonlinear flows. Approximately, it is the ratio of work per mass done by buoyancy ( $\Delta b D_p$ ) and the kinetic energy per mass of the plume ( $v_p^2$ ). Therefore,  $R_b \lesssim 1$  offers little resistance to penetration,  $R_b > 1$  represents a stiff boundary, and where  $R_b \sim 1$ , the work done by buoyancy balances the plume's kinetic energy, causing it to turn around. Hence,  $R_b$  is appropriate in characterizing the penetration of downdrafts into the underlying stable layers.

To estimate scales and trends, we approximate the integral in Equation (23), giving

$$\Delta b \sim N^2 D_p, \quad (25)$$

and we assume that  $R_b \sim 1$ , which we argued above is where buoyancy balances the plume's kinetic energy and gives the turn-around point. This gives  $(N D_p / v_p)^2 \sim 1$ , or

$$D_p \sim \frac{v_p}{N}. \quad (26)$$

We note that this scaling is similar to the gravity wave displacement amplitude derived by Meakin & Arnett (2007a), which they derive by equating the gravity wave pressure fluctuations to the ram pressure of the convective eddies at the boundary. An estimate of the characteristic timescale is given by the velocity divided by the acceleration,  $t_p \sim v_p / \Delta b$ . Substituting in Equations (25) and (26) gives<sup>11</sup>

$$f_p \sim \frac{N}{2\pi}. \quad (27)$$

Interestingly, this characteristic frequency is insensitive to the plume velocity and penetration depth. Rather,  $f_p$  is most sensitive to the buoyancy frequency at the turning point ( $N_{\text{turn}}$ ).

Although the above analysis suggests that the characteristic frequency is independent of  $v_p$ , the amplitude of the GW strain is directly dependent upon these velocities. Very roughly, the GW strain is

$$h_+ \sim \frac{4\pi G}{Dc^4} \rho f_p v_p r^3 \Delta r \Delta \mu, \quad (28)$$

where we use Equations (12) and (13),  $\Delta \mu$  is the finite difference approximation of  $d \cos \theta$ , and we assume that  $\partial(\rho v_p)/\partial t \sim \rho \partial v_p / \partial t$  and that  $\partial v_p / \partial t \sim f_p v_p$ . Figure 10 compares  $h_+ D$  with the maximum downward plume speed below 120 km,  $v_p$ , as a function of time after bounce. The spikes in  $v_p$  correspond to the strongest plumes that strike the PNS "surface," and the baseline, below which  $v_p$  does not dip, shows the time-averaged accretion of material onto the PNS. As the PNS accumulates more mass, exerting stronger gravitational forces, the background and plume velocities evolve upward slightly until  $\sim 550$  ms after bounce. At this time, the motions in the postshock-convection/SASI region increase dramatically, leading to a significant rise in  $v_p$ . After the start of explosion ( $\gtrsim 800$  ms), it no longer makes sense to define a plume velocity, since the GW signal during explosion is dominated by explosion dynamics. Hence, we do not show  $v_p$  after  $\sim 800$  ms.

Initially, prompt convection dominates the signal and  $v_p$  is not relevant. As prompt convection settles to steady-state convection, the plumes become more relevant. From  $\sim 150$  ms to  $\sim 550$  ms, both  $v_p$  and the GW amplitude are low, but as  $v_p$  grows so does the GW amplitude. Strikingly, the increase in GW wave strain at  $\sim 600$  ms coincides with the rise in  $v_p$ .

<sup>11</sup> The factor of  $2\pi$  arises because the definition of  $t_p$  is similar to the  $\sigma_t$  in  $\exp(-t^2/(2\sigma_t^2))$ , and the Fourier transform of this Gaussian is another Gaussian with width  $\sigma_f = 1/(2\pi\sigma_t)$ .

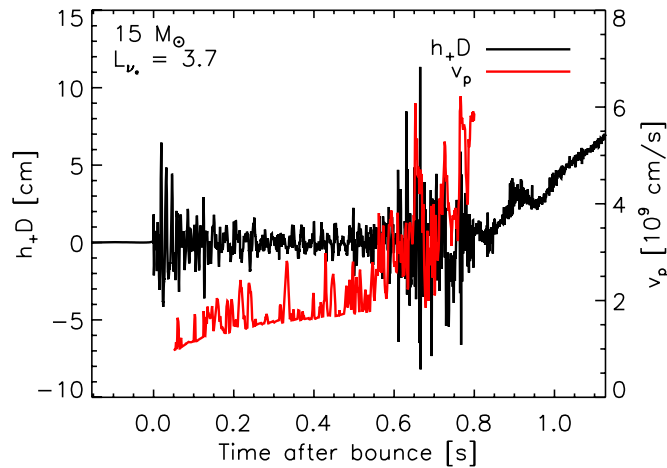


**Figure 10.** Comparison of  $h_+D$  with the maximum downward plume speed below 120 km,  $v_p$ , vs. time after bounce. The increase in GW wave strain at  $\sim 600$  ms coincides with the rise in  $v_p$ , and many spikes in  $h_+D$  coincide with rapid changes in  $v_p$ . A rough estimate of  $h_+D$  using these plume speeds gives  $\sim 5$  cm, which is consistent with the calculated GW strain (see the text in Section 3.4).

(A color version of this figure is available in the online journal.)

In fact, many, but not all, spikes in  $h_+D$  coincide with rapid changes in  $v_p$ . Furthermore after  $\sim 600$  ms, substituting values for typical flows near the boundary (e.g.,  $\rho \sim 10^{11}$  g cm $^{-3}$ ,  $v_p \sim 4 \times 10^9$  cm s $^{-1}$ ,  $r \sim 60$  km,  $\Delta r \sim D_p \sim 20$  km,  $f_p \sim 300$  Hz, and  $\Delta\mu \sim D_p/(\pi r)$ ) into Equation (28) gives  $h_+D \sim 5$  cm, which is the order of magnitude of the GW strain.

Figures 11 and 12 depict the buoyancy frequency,  $N$  (solid blue line, online version),  $(GM_r/r^3)^{1/2}$  (dashed purple line, online version), and the radial velocity,  $v_r$  (black points), as a function of radius at 300 and 620 ms after bounce for the 2D simulation that uses the  $15 M_\odot$  progenitor model and  $L_{v_e} = 3.7 \times 10^{52}$  erg s $^{-1}$ . The velocities clearly show (from large to small radii), spherical infall, the asymmetric shock, the postshock-convection/SASI region, a stable layer, and PNS convection. At 300 ms (Figure 11), the dynamics are dominated by postshock-convection and mild SASI oscillations, while at 620 ms, the SASI oscillations have increased substantially. Roughly, the buoyancy frequency scales with the average density, Equation (22). However, at the core, the spatial derivatives, and therefore  $N$ , approach zero. In the regions of PNS convection ( $\sim 20$  to  $\sim 40$  km) and postshock convection ( $\gtrsim 100$  km),  $N^2$  is negative. Green line segments in both figures indicate the regions that are unstable to convection by the Ledoux condition in 1D simulations, and the penetration depths,  $D_p$ , which are computed by integrating the plume's equation of motion, are labeled and indicated by an orange line. At 300 and 620 ms after bounce,  $D_p$  at the base of the region of postshock convection is  $\sim 25$  and  $\sim 39$  km, respectively. These analytic penetration depths agree with those obtained from the numerical simulations. Note that the boundaries of PNS convection in the 2D simulations coincide with the boundaries given by the Ledoux condition. This is due to the fact that the relatively large buoyancy frequency and small convective speeds imply very small overshoot depths (Equation (26)) at the edges of PNS convection. The plume frequencies,  $f_p$ , obtained from the HWHM timescale of the acceleration pulses, are  $\sim 196$  Hz at 300 ms and  $\sim 272$  Hz at 620 ms.

To better understand the contributions to  $f_p$ , we plot in Figure 13 the characteristic frequency ( $f_p$ ), the buoyancy frequency at  $D_p$  ( $N_{\text{turn}}/(2\pi)$ ), and  $(GM_r/r^3)^{1/2}/(2\pi)$  at  $D_p$  as

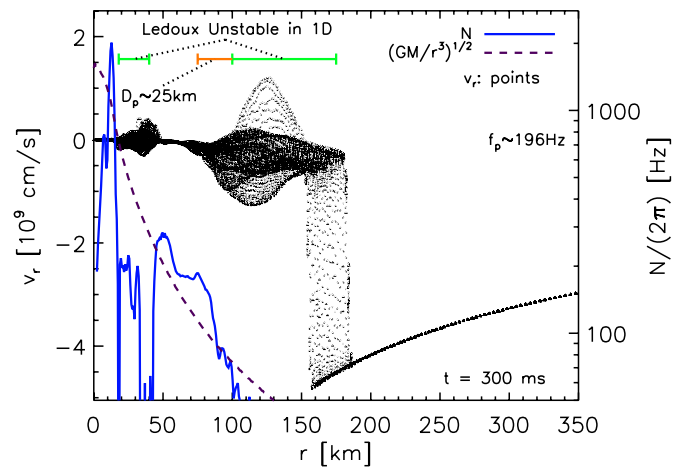


**Figure 11.** Buoyancy frequency,  $N$  (blue-solid line, online version),  $(GM_r/r^3)^{1/2}$  (purple-dashed line, online version), and the radial velocity,  $v_r$  (black points), vs. radius at 300 ms after bounce for the 2D simulation that uses the  $15 M_\odot$  progenitor model and  $L_{v_e} = 3.7 \times 10^{52}$  erg s $^{-1}$ . Starting at larger radii, the velocity points show spherical infall, an asymmetric shock, postshock convection/SASI, a stable layer, the PNS convection, and a stable inner core. At this time, the dynamics are dominated by postshock-convection and mild SASI oscillations. The convection regions are characterized by two regions: (1) that which is unstable by the Ledoux condition (green lines, online version) and (2) the region of overshoot below the postshock-convection region (orange line, online version). The penetration depth,  $D_p$ , associated with overshoot is computed by integrating the plume's equation of motion and finding the depth at which the plume turns around. The plume frequency,  $f_p$ , obtained from the HWHM timescale of the acceleration pulses, is  $\sim 196$  Hz.

(A color version of this figure is available in the online journal.)

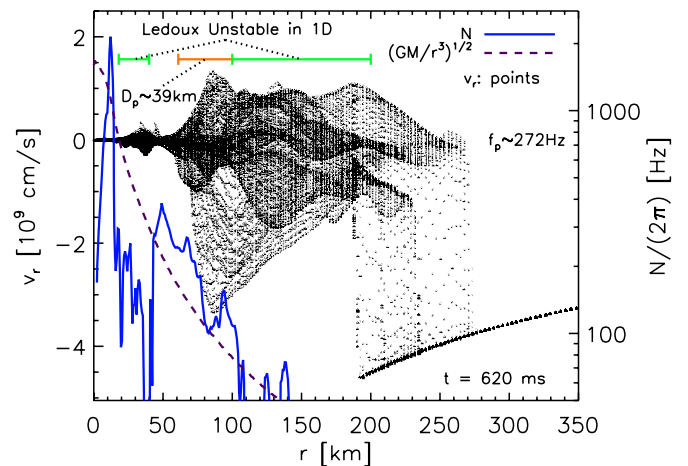


**Figure 12.** Similar to Figure 11, except that  $t = 620$  ms. At this time, the SASI oscillations are much stronger, resulting in a higher penetration depth of  $D_p \sim 39$  km. Because  $N$  has also increased, the characteristic frequency,  $f_p$ , is higher at 272 Hz.

(A color version of this figure is available in the online journal.)

a function of time after bounce. Strikingly,  $f_p$  and  $N_{\text{turn}}/(2\pi)$  agree quantitatively. Since  $f_p$  is calculated using the equation of motion and is independent of the approximations and assumptions that led to Equation (27), the fact that  $f_p$  is nearly equal to  $N_{\text{turn}}/(2\pi)$  for all times provides implicit confirmation of our approximations and assumptions in deriving the analytic result. Furthermore, we calculated the ratio  $N_{\text{turn}}D_p/v_p$  (the square root of  $R_b$  after inserting the approximation that  $\Delta b \sim N^2 D_p$ ) for all models (Figure 14), found that its value is around 1.5–2, and that it changes less than 30% during the simulation. This validates both the assumption that  $R_b \sim 1$  characterizes where the plumes turn around and the approximation that  $\Delta b \sim N^2 D_p$ .

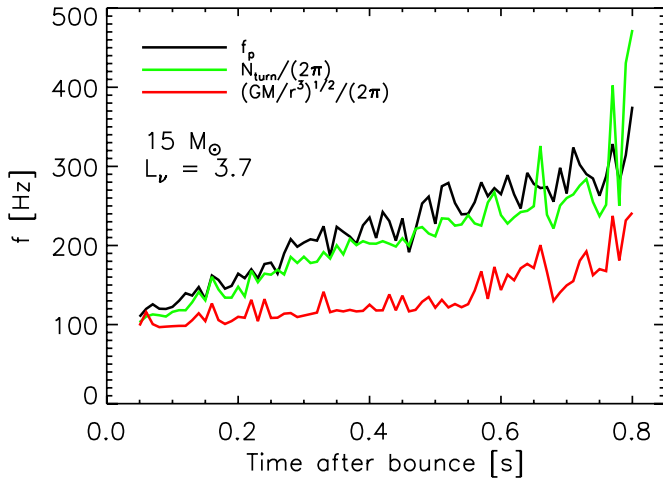


**Figure 13.** Shown are characteristic plume frequency,  $f_p$ , the buoyancy frequency at  $D_p$ ,  $N_{\text{turn}}$ , and  $(GM_r/r^3)^{1/2}$  at  $D_p$  as a function of time after bounce for the 2D simulation using the  $15 M_\odot$  progenitor and  $L_{\nu_e} = 3.7 \times 10^{52} \text{ erg s}^{-1}$ . Initially, all three coincide. However, while  $N_{\text{turn}}$  tracks the time evolution of  $f_p$ ,  $(GM_r/r^3)^{1/2}$  diverges from the other two measures. This indicates that while  $(GM_r/r^3)^{1/2}$  (which is related to the compactness of the PNS) sets the general frequency scale, the local logarithmic gradients at the penetration depth are just as important in determining  $N_{\text{turn}}$ .

(A color version of this figure is available in the online journal.)

Initially, all three measures of frequency in Figure 13 coincide. However, while  $N_{\text{turn}}/(2\pi)$  tracks the time evolution of  $f_p$ ,  $(GM_r/r^3)^{1/2}/(2\pi)$  diverges from the other two measures. By plotting both  $N_{\text{turn}}$  and  $(GM_r/r^3)^{1/2}$ , which is the inverse free-fall time, we highlight global (inverse free-fall time) and local (difference of logarithmic derivatives) properties of the PNS that contribute to Equation (22). The inverse free-fall time is proportional to the square root of the average density (compactness), which is strongly dependent upon the dense-matter EOS. Marek et al. (2009) reported a change in peak GW frequency with stiff and soft dense-matter equations of state, though they make reference to only compact PNSs without explaining the timescales in the context of the buoyancy frequency. Figure 13 shows that both the global compactness and the local gradients at the penetration depth are important in determining  $N_{\text{turn}}$ . These local gradients are strongly dependent upon the details of deleptonization and cooling. Therefore, the time evolution of the characteristic frequencies is a strong function of both the dense-matter EOS in the PNS below the boundary layer and the local microphysics of the boundary layer itself.

Figure 9 compares  $f_p$  with the spectrogram,  $dE_{\text{GW}}^*/df$  (Equation (20)), of the simulation using the  $15 M_\odot$  progenitor and  $L_{\nu_e} = 3.7 \times 10^{52} \text{ erg s}^{-1}$ . From bounce until explosion, the frequency at peak power coincides with  $f_p$ . This strong correlation persists whether prompt convection, convection, or the SASI are the dominant instabilities and implies that the plume's buoyant deceleration determines the characteristic GW frequency at all times before explosion.

In Figure 15, we plot  $f_p$  as a function of time after bounce for all 2D simulations. Each shade (color in the online version) represents a set of simulations with the same progenitor model but different  $L_{\nu_e}$ : black for  $12 M_\odot$ , blue (online) for  $15 M_\odot$ , green (online) for  $20 M_\odot$ , and red (online) for  $40 M_\odot$ . As in Figure 9, careful inspection of these  $f_p$ -time curves show that they agree with the trends of peak frequency in the GW spectrograms, Figure 8. For simulations that use the same progenitor model, their  $f_p$  evolutions are practically indistinguishable. The only differences are that the higher luminosity simulations explode

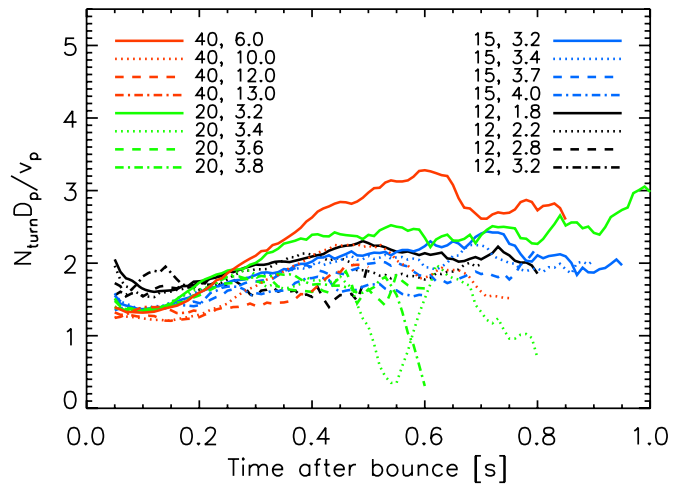


**Figure 14.** Ratio  $N_{\text{turn}} D_p / v_p$ , which is the square root of  $R_b$  after inserting the approximation that  $\Delta b \sim N^2 D_p$ , vs. time after bounce for all 2D simulations listed in Table 1. Each line is labeled by the progenitor mass and neutrino luminosity used. Each shade (color in the online version) represents a set of simulations using the same progenitor model: black for  $12 M_\odot$ , blue (online) for  $15 M_\odot$ , green (online) for  $20 M_\odot$ , and red (online) for  $40 M_\odot$ . The style of line corresponds to the neutrino luminosity used, but note that the range of neutrino luminosities for a set of models that use the same progenitor mass is different from another set. This ratios are  $\sim 1.5$  to  $\sim 2$ , and change less than 30% during the simulations. This validates both the assumption that  $R_b$  is of order 1 where the plumes turn around and the approximation that  $\Delta b \sim N^2 D_p$ .

(A color version of this figure is available in the online journal.)

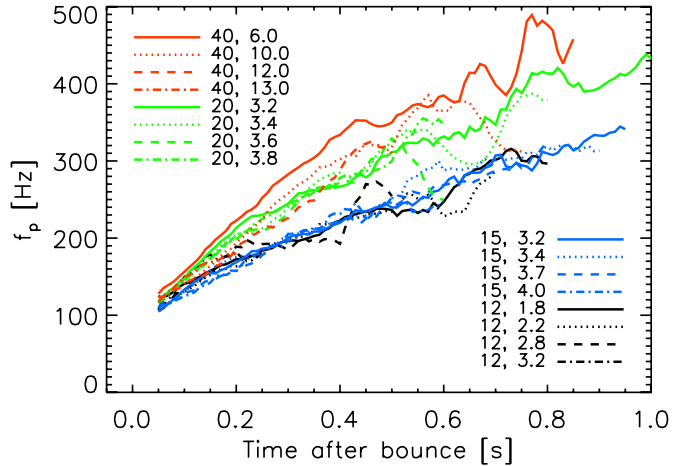


**Figure 15.** Characteristic plume frequency,  $f_p$ , as a function of time after bounce for all 2D simulations listed in Table 1. The shading (color in the online version) and line schemes are the same as in Figure 14. For simulations that use the same progenitor model, the  $f_p$ -time evolutions are close. The only differences are that the higher luminosity simulations explode earlier (the end of  $f_p$ -time curves mark the approximate time of explosion) and consequently have lower frequencies at explosion. In general, the higher mass progenitors produce higher frequencies, with the exception that the 12 and  $15 M_\odot$  models have very similar  $f_p$ -time curves.

(A color version of this figure is available in the online journal.)

earlier (the end of  $f_p$ -time curves mark the approximate time of explosion) and consequently have lower frequencies at explosion. In general, the higher mass progenitors produce higher frequencies, with the exception that the 12 and  $15 M_\odot$  models have very similar  $f_p$ -time curves.

Yoshida et al. (2007) also investigated the interaction between the plumes of postshock-convection/SASI region and the stable layers below it. Their motivation was to investigate the excitation of PNS core  $g$ -modes, which are vital for the success of the acoustic mechanism (Burrows et al. 2006, 2007b), by these

plumes. They concluded that the driving pressure perturbations had frequencies that are much too low to cause excitation of the PNS core  $g$ -modes. As a result, they suggest that core  $g$ -mode excitation is inefficient, rather the core  $g$ -modes are forced oscillations. However, their analysis relied upon the power spectrum of pressure perturbations at the base of 2D simulations with inner boundaries at  $\sim 50$  km. While they attempt to handle the subsonic outflow through this inner boundary consistently, they are forced to set the radial velocity at this inner boundary to maintain the subsonic structure above the boundary. This boundary condition certainly limits the motions at the base of their calculations, and their unfortunate choice of the location of their inner boundary is exactly where the plume's motions are most important for exciting core  $g$ -modes.

Furthermore, there is some confusion in the literature concerning the appropriate frequencies and excitation mechanism for the core  $g$ -modes. While pressure perturbations play some role in exciting core  $g$ -modes, it is well known that buoyancy is the dominant driving force in  $g$ -waves (e.g., Unno et al. 1989, Chapter III, Section 13). Therefore, velocity perturbations, which result from both pressure and buoyancy forces, are more relevant in characterizing the perturbation spectrum at the surface of the PNS. The power spectrum of the pressure perturbations is most useful at highlighting the sounds waves that are emitted by oscillating PNS. Furthermore, in their discussion of the relevant frequencies, Yoshida et al. (2007) reference the  $\sim 30$  to  $\sim 80$  Hz shock-oscillation frequencies in Table 1 of Burrows et al. (2007b) and conclude that motions associated with these frequencies are much too low to excite core  $g$ -modes which typically have frequencies around 300 Hz. However, these shock-oscillation frequencies are not relevant in driving oscillations at the surface of the PNS. Rather, we have shown that the characteristic frequencies associated with the plume impulses are most relevant and have frequencies that are very similar to the core  $g$ -mode frequencies. Though we address neither the acoustic mechanism nor the core  $g$ -modes in this paper, in light of our characteristic frequency analysis, it is possible that the plumes associated with postshock convection/SASI excite core  $g$ -mode oscillations (Burrows et al. 2007b).

#### 4. DISCUSSION AND SUMMARY

In this paper, we present a systematic study of the GW emission from 2D core-collapse supernova simulations in the context of the convection/SASI-aided neutrino mechanism. Using a range of progenitor masses (12, 15, 20, and  $40 M_{\odot}$ ) and neutrino luminosities, we investigate the effects of core structure and explosion on the GW signal. In addition to GW signatures of prompt convection, PNS and postshock convection, and the SASI, we characterize the GW signal of asymmetric mass ejections during explosions and identify the signatures of explosion that current and near-future GW observatories may detect. Moreover, we propose that the characteristic GW frequencies and amplitudes are determined by the deceleration of postshock-convective/SASI plumes by the buoyantly stable layers below. We provide gravitational waveforms from all simulated models at <http://stellarcollapse.org/gwcatalog/murphyetal2009>.

For all exploding models, we highlight four distinct phases in the matter GW strain,  $h_+D$ . Figure 2 shows that just after bounce, prompt convection leads to a burst in GW emission with  $h_+D$  reaching  $\sim 5$  cm and having a frequency of  $\sim 100$  Hz. This lasts for  $\sim 50$  ms or so before steady-state convection is established and  $h_+D$  settles down to  $\sim 1$  cm. As the SASI increases in vigor,  $h_+D$  increases to  $\sim 10$  cm and is punctuated with strong spikes

that are strongly correlated with downdrafts striking the PNS “surface.” From bounce until explosion, the peak frequency of the GW emission rises from  $\sim 100$  Hz to  $\sim 300$ – $400$  Hz, with higher values corresponding to higher mass progenitors and/or later explosion times (lower neutrino luminosities).

For a few simulations, the transition to strong SASI and GW emission is initiated by a substantial drop in accretion rate, which is caused by an abrupt change in density/entropy at the base of the progenitor's oxygen-burning shell (Murphy & Burrows 2008b). The fact that the correlation is weak precludes using individual GW detections to investigate the location of this entropy edge, but a large sample of detections could provide statistical constraints. However, if convection/SASI is the only GW emission mechanism, detection of CCSNe by current and near-future GW detectors is limited to our galaxy. Within this radius, the rate of CCSNe is roughly one per century (e.g., van den Bergh & Tammann 1991; Cappellaro et al. 1999), a rate that is far too low to build a statistical sample. Such a sample of GW detections from CCSNe is only feasible if they can be detected with distances out to  $\sim 4$ – $5$  Mpc, where the rate increases to  $\sim 1$ – $2$  per year (e.g., Ando et al. 2005). Third generation observatories, e.g., the proposed Einstein Telescope,<sup>12</sup> or even more sensitive detectors may be required to study the GW emission from convection/SASI in CCSNe out to  $\sim 4$ – $5$  Mpc.

As explosion ensues, the SASI and neutrino-driven convection above the neutrinosphere subside, causing the rapid oscillations and large spikes in the GW strain to reduce in amplitude. In their stead, aspherical mass ejection results in a slow, but sometimes large, monotonic rise in the GW strain. For spherical explosions, the strain settles back to zero after the onset of explosion, while the strain rises to positive values for prolate explosions and drops to negative values for oblate explosions. This is similar to the “burst with memory” GW signal that asymmetric neutrino emission produces (Braginskii & Thorne 1987; Burrows & Hayes 1996; Müller & Janka 1997). Consequently, the peak GW power emitted moves from  $\sim 300$ – $400$  Hz to  $\sim 10$ s of Hz. Initial and Enhanced LIGO sensitivity at low frequencies inhibit direct detection of this explosion signature. Although the improved sensitivity of Advanced LIGO at lower frequencies might enable direct detection of the explosion signature, the abrupt reduction in power at the higher frequencies is the most obvious signature of explosion for the first generation detectors.

We stress that this reflects the integrated,  $\ell = 2$  morphology of the mass during the explosion. The snapshots of entropy in Figure 4 show that while the general morphology of the matter may be prolate, oblate, or spherical, the entropy and composition distributions are much more complex. So, while the shock wave may be spherical, the composition distributions are likely to be aspherical. The spherical shock wave but asymmetric Fe and Si ejecta distributions in the Cas A supernova remnant, might be a prime example of this (DeLaney et al. 2009).

These monotonic changes due to asymmetric matter ejection will be superposed on the large secular changes due to asymmetric neutrino emission (Burrows & Hayes 1996; Müller & Janka 1997; Müller et al. 2004; Marek et al. 2009). If the timescales and amplitudes are similar, then it will be difficult to distinguish between the neutrino and asymmetric matter ejection GW signals. Simulations that employ more consistent neutrino transport for several 100 ms past explosion are necessary to resolve this issue. Regardless, for CCSNe in which convection/SASI is the dominant source of GWs, distinguishing among prolate, oblate,

<sup>12</sup> <http://www.et-gw.eu>

or spherical explosions will require direct detection of the GW amplitude to enable a determination of the sign of the amplitude. This will only be possible if a very close post-main-sequence star such as Betelgeuse, which is a mere  $197 \pm 45$  pc away (Harper et al. 2008), explodes in the near future. Otherwise, the distances to typical Galactic SNe ( $\sim 10$  kpc), detector characteristics, and their sensitivity to frequencies  $\gtrsim 50$  Hz imply that the low-frequency “memory” signal will not be detected, and the signature of explosion will be the abrupt reduction in GW power.

Except for the explosion signature, Marek et al. (2009) report similar characteristics in the GW strain. The evolution in frequency from  $\sim 100$  Hz just after bounce to larger frequencies at later times agrees with the results of Marek et al. (2009). In fact, our higher frequencies are consistent with the calculations that use a stiff EOS, but roughly half for those reported for their softer EOS simulation. Kotake et al. (2007, 2009), on the other hand, report only one phase of weak GW emission exhibiting gradual growth and one characteristic frequency at  $\sim 100$  Hz. We suspect that the idealized initial conditions and omission of the inner 50 km precludes them from simulating many of the features that we and Marek et al. (2009) identify.

While the total GW emission originates from regions including the PNS convection at depth, the stable layer above it, and the base of the outer convective and SASI regions, we find that the characteristic GW frequencies and amplitudes are, for the most part, established by the interaction of postshock-convection/SASI region and the stable layers below. As plumes in the convective/SASI region fall toward the stable layer below, momentum carries their motion beyond the lower boundary of convection as defined by the Ledoux condition. As they penetrate the stable regions, the plumes experience a buoyancy acceleration upward. It is this impulse that gives rise to the GW emission. The pulse width has a characteristic frequency,  $f_p$ , that corresponds to the peak power of GW emission, and we show that  $f_p$  is insensitive to the plume velocity. Instead,  $f_p$  is set by the buoyancy frequency where the plume reverses its downward motion,  $f_p \sim N_{\text{turn}}/(2\pi)$ . Moreover, the conditions during this deceleration are of the correct order of magnitude to explain the GW strain amplitude. In particular, we show that the amplitude is directly proportional to the plume velocity,  $h_+ \propto f_p v_p \propto N_{\text{turn}} v_p$ .

Since  $f_p$  is set by  $N_{\text{turn}}$ , the frequency at peak GW power gives direct information on the core structure. This is not too surprising. In fact, using soft and stiff dense-matter EOSs, Marek et al. (2009) find higher peak frequencies for the former, which they attribute to the compactness of the PNS. While compactness certainly influences  $N_{\text{turn}}$ , we emphasize that local conditions at the PNS “surface” and their evolution are just as important in determining the characteristic GW frequencies. As a point of clarification, we find that sloshing and turnover timescales do not set the characteristic GW frequency. Assuming that  $f_p$  is proportional to  $v_p$  divided by a length scale such as an eddy size, one might conclude that  $f_p$  is directly proportional to the plume speed. This contradicts our earlier finding that  $f_p$  is dependent only on the core structure. However, in Section 3.4, we show that the relevant length scale is the deceleration length, or penetration depth,  $D_p$ , and that  $D_p \sim v_p/N$ , giving the result that  $f_p$  is proportional to  $N$  and independent of  $v_p$ .

In general, we find that more massive progenitors have higher  $f_p$  at a given time, though the 12 and 15  $M_\odot$  models show similar  $f_p$  evolution. Interestingly, our simulations show that the  $f_p$  versus time evolution for a given progenitor model

is independent of the neutrino luminosity. The fact that the characteristic frequency at explosion is dependent upon neutrino luminosity is simply due to the fact that higher luminosity simulations explode earlier in an otherwise similar  $f_p$ -time evolution.

Though we state that our conclusions are qualitatively valid, we have made several assumptions that enabled timely calculation of the simulations in this paper. The effects of neutrino transport were approximated by local heating and cooling functions, azimuthal symmetry was assumed, though nature is inherently 3D, and we used spherical Newtonian gravity rather than a full general relativistic treatment.

Differences between 2D and 3D simulations are likely to matter quantitatively. For one, in steady-state stellar convection, the eddies are larger and have faster speeds in 2D simulations (Arnett et al. 2009; Meakin & Arnett 2007b; and the references therein). Although we have demonstrated that the characteristic frequencies are unlikely to be affected, the GW strain amplitude is directly proportional to the plume speed and will be affected. However, these arguments are for convection alone; they ignore the fact that in the gain region, convection, the SASI, and advection are equally important. For example, the fact that we can explain the characteristic GW frequencies by considering the interaction of convective plumes with neighboring buoyant layers implies that convection is important. On the other hand, the rapid rise in plume velocities as the SASI becomes nonlinear is a clear indication that the SASI is equally important. Even though simulations are beginning to explore the 3D aspects of the SASI (Iwakami et al. 2008, 2009; Kotake et al. 2009) and advection-modified convection has been explored in the linear regime (Foglizzo et al. 2006), there has yet to be a complete analysis of nonlinear convection that is modified by either. Furthermore, Murphy & Burrows (2008b) have noted that the accretion through the convective/gain region imposes an inherent asymmetry in the convective flow. While some matter advects quickly through the convective/gain region (these are the downdrafts/plumes), some lingers for very long times. To what degree do these effects hold in 3D simulations? As yet the similarities and differences are not obvious and remain an interesting and important avenue of research for core-collapse simulations.

Though 3D effects may not alter the characteristic frequencies, including general relativity and consistent neutrino transport undoubtedly will. With general relativistic corrections, the PNS structure is more compact, leading to higher characteristic frequencies. Without proper treatment of neutrino transport, in particular,  $\nu_\mu$  and  $\nu_\tau$  emission, the PNSs in our simulations do not lose energy and shrink as they should. Including these effects should increase  $(GM_r/r^3)^{1/2}$  over time, further increasing  $f_p$  in our simulations. Furthermore, the neutrino transport is important in determining the structure, and, hence, buoyancy frequency, at the surface of the PNS. Therefore, to obtain a reliable and quantitative mapping between the model characteristic frequencies from postshock-convection/SASI motions and those observed by GW detectors such as LIGO, approximations to GR, and the neutrino transport that more faithfully mimic nature are required in future simulations.

We acknowledge helpful discussions with and input from Casey Meakin and Eric Agol. J.W.M. is supported by an NSF Astronomy and Astrophysics Postdoctoral Fellowship under award AST-0802315. C.D.O. is supported by a Sherman Fairchild postdoctoral fellowship at Caltech, by an NSF award

under grant number AST-0855535, and by an Otto Hahn Prize awarded by the Max Planck Society. A.B. acknowledges support for this work from the Scientific Discovery through Advanced Computing (SciDAC) program of the DOE, under grant number DE-FG02-08ER41544. We acknowledge that the work reported in this paper was substantially performed at the TIGRESS high performance computer center at Princeton University which is jointly supported by the Princeton Institute for Computational Science and Engineering and the Princeton University Office of Information Technology and on the ATHENA cluster at the University of Washington. Further computations were performed on the NSF Teragrid under grant TG-MCA02N014, on machines of the Louisiana Optical Network Initiative under grant LONI\_NUMREL04, and at the National Energy Research Scientific Computing Center (NERSC), which is supported by the Office of Science of the US Department of Energy under contract DE-AC03-76SF00098.

## REFERENCES

- Abbott, B. P., et al. (LIGO Scientific Collaboration) 2009, *Rep. Prog. Phys.*, **72**, 076901
- Ando, S., Beacom, F., & Yüksel, H. 2005, *Phys. Rev. Lett.*, **95**, 171101
- Arnett, D., Meakin, C., & Young, P. A. 2009, *ApJ*, **690**, 1715
- Bethe, H. A., & Wilson, J. R. 1985, *ApJ*, **295**, 14
- Blanchet, L., Damour, T., & Schaefer, G. 1990, *MNRAS*, **242**, 289
- Blondin, J. M., & Mezzacappa, A. 2006, *ApJ*, **642**, 401
- Blondin, J. M., Mezzacappa, A., & DeMarino, C. 2003, *ApJ*, **584**, 971
- Braginskii, V. B., & Thorne, K. S. 1987, *Nature*, **327**, 123
- Bretherton, C. S., et al. 1999, *Q. J. R. Meteorol. Soc.*, **128**, 2663
- Bruenn, S. W. 1985, *ApJS*, **58**, 771
- Bruenn, S. W. 1989, *ApJ*, **340**, 955
- Buras, R., Janka, H.-T., Rampp, M., & Kifonidis, K. 2006a, *A&A*, **457**, 281
- Buras, R., Rampp, M., Janka, H.-T., & Kifonidis, K. 2003, *Phys. Rev. Lett.*, **90**, 241101
- Buras, R., Rampp, M., Janka, H.-T., & Kifonidis, K. 2006b, *A&A*, **447**, 1049
- Burrows, A., Dessart, L., & Livne, E. 2007a, in *AIP Conf. Ser.* 937, *Supernova 1987A: 20 Years After: Supernovae and Gamma-Ray Bursters*, ed. S. Immler & R. McCray (Melville, NY: AIP), 370
- Burrows, A., Dessart, L., Livne, E., Ott, C. D., & Murphy, J. 2007b, *ApJ*, **664**, 416
- Burrows, A., & Fryxell, B. A. 1992, *Science*, **258**, 430
- Burrows, A., & Hayes, J. 1996, *Phys. Rev. Lett.*, **76**, 352
- Burrows, A., Hayes, J., & Fryxell, B. A. 1995, *ApJ*, **450**, 830
- Burrows, A., Livne, E., Dessart, L., Ott, C. D., & Murphy, J. 2006, *ApJ*, **640**, 878
- Burrows, A., Livne, E., Dessart, L., Ott, C. D., & Murphy, J. 2007c, *ApJ*, **655**, 416
- Burrows, A., Young, T., Pinto, P., Eastman, R., & Thompson, T. A. 2000, *ApJ*, **539**, 865
- Cappellaro, E., Evans, R., & Turatto, M. 1999, *A&A*, **351**, 459
- DeLaney, T., et al. 2009, *BAAS*, **41**, 377
- Dessart, L., Burrows, A., Livne, E., & Ott, C. D. 2006, *ApJ*, **645**, 534
- Dessart, L., Burrows, A., Livne, E., & Ott, C. D. 2008, *ApJ*, **673**, L43
- Dimmelmeier, H., Font, J. A., & Müller, E. 2002, *A&A*, **393**, 523
- Dimmelmeier, H., Ott, C. D., Janka, H.-T., Marek, A., & Müller, E. 2007, *Phys. Rev. Lett.*, **98**, 251101
- Dimmelmeier, H., Ott, C. D., Marek, A., & Janka, H.-T. 2008, *Phys. Rev. D*, **78**, 064056
- Fernando, H. J. S. 1991, *Annu. Rev. Fluid Mech.*, **23**, 455
- Fernando, H. J. S., & Hunt, J. C. R. 1997, *J. Fluid Mech.*, **347**, 197
- Finn, L. S., & Evans, C. R. 1990, *ApJ*, **351**, 588
- Flanagan, É. É., & Hughes, S. A. 1998, *Phys. Rev. D*, **57**, 4535
- Foglizzo, T. 2001, *A&A*, **368**, 311
- Foglizzo, T. 2002, *A&A*, **392**, 353
- Foglizzo, T. 2009, *ApJ*, **694**, 820
- Foglizzo, T., Galletti, P., Scheck, L., & Janka, H.-T. 2007, *ApJ*, **654**, 1006
- Foglizzo, T., Scheck, L., & Janka, H.-T. 2006, *ApJ*, **652**, 1436
- Foglizzo, T., & Tagger, M. 2000, *A&A*, **363**, 174
- Gustafson, E., Shoemaker, D., Strain, K., & Weiss, R. 1999, LSC White Paper on Detector Research and Development (LIGO Tech. Rep. T990080-00-D)
- Harper, G. M., Brown, A., & Guinan, E. F. 2008, *AJ*, **135**, 1430
- Heger, A., Woosley, S. E., & Spruit, H. C. 2005, *ApJ*, **626**, 350
- Herant, M., Benz, W., Hix, W. R., Fryer, C. L., & Colgate, S. A. 1994, *ApJ*, **435**, 339
- Hirschi, R., Meynet, G., & Maeder, A. 2004, *A&A*, **425**, 649
- Iwakami, W., Kotake, K., Ohnishi, N., Yamada, S., & Sawada, K. 2008, *ApJ*, **678**, 1207
- Iwakami, W., Kotake, K., Ohnishi, N., Yamada, S., & Sawada, K. 2009, *ApJ*, **700**, 332
- Janka, H.-T. 2001, *A&A*, **368**, 527
- Janka, H.-T., & Müller, E. 1995, *ApJ*, **448**, L109
- Janka, H.-T., & Müller, E. 1996, *A&A*, **306**, 167
- Keil, W., Janka, H.-T., & Mueller, E. 1996, *ApJ*, **473**, L111
- Kitaura, F. S., Janka, H.-T., & Hillebrandt, W. 2006, *A&A*, **450**, 345
- Kotake, K., Iwakami, W., Ohnishi, N., & Yamada, S. 2009, *ApJ*, **697**, L133
- Kotake, K., Ohnishi, N., & Yamada, S. 2007, *ApJ*, **655**, 406
- Kotake, K., Yamada, S., & Sato, K. 2003, *ApJ*, **595**, 304
- Kotake, K., Yamada, S., Sato, K., Sumiyoshi, K., Ono, H., & Suzuki, H. 2004, *Phys. Rev. D*, **69**, 124004
- Laming, J. M. 2007, *ApJ*, **659**, 1449
- Liebendörfer, M. 2005, *ApJ*, **633**, 1042
- Liebendörfer, M., Mezzacappa, A., & Thielemann, F. 2001a, *Phys. Rev. D*, **63**, 104003
- Liebendörfer, M., Mezzacappa, A., Thielemann, F., Messer, O. E., Hix, W. R., & Bruenn, S. W. 2001b, *Phys. Rev. D*, **63**, 103004
- Liebendörfer, M., Rampp, M., Janka, H.-T., & Mezzacappa, A. 2005, *ApJ*, **620**, 840
- Livne, E. 1993, *ApJ*, **412**, 634
- Livne, E., Burrows, A., Walder, R., Lichtenstadt, I., & Thompson, T. A. 2004, *ApJ*, **609**, 277
- Marek, A., & Janka, H.-T. 2009, *ApJ*, **694**, 664
- Marek, A., Janka, H.-T., & Müller, E. 2009, *A&A*, **496**, 475
- Mazurek, T. J. 1982, *ApJ*, **259**, L13
- Meakin, C. A., & Arnett, D. 2007a, *ApJ*, **665**, 690
- Meakin, C. A., & Arnett, D. 2007b, *ApJ*, **667**, 448
- Misner, C. W., Thorne, K. S., & Wheeler, J. A. 1973, *Gravitation* (San Francisco: Freeman)
- Mönchmeyer, R., Schäfer, G., Müller, E., & Kates, R. 1991, *A&A*, **246**, 417
- Müller, E. 1982, *A&A*, **114**, 53
- Müller, E., & Janka, H.-T. 1997, *A&A*, **317**, 140
- Müller, E., Rampp, M., Buras, R., Janka, H.-T., & Shoemaker, D. H. 2004, *ApJ*, **603**, 221
- Murphy, J. W., & Burrows, A. 2008a, *ApJS*, **179**, 209
- Murphy, J. W., & Burrows, A. 2008b, *ApJ*, **688**, 1159
- Obergaulinger, M., Aloy, M. A., & Müller, E. 2006, *A&A*, **450**, 1107
- Ohnishi, N., Kotake, K., & Yamada, S. 2006, *ApJ*, **641**, 1018
- Ott, C. D. 2009a, *Class. Quantum Grav.*, **26**, 204015
- Ott, C. D. 2009b, *Class. Quantum Grav.*, **26**, 063001
- Ott, C. D., Burrows, A., Dessart, L., & Livne, E. 2006a, *Phys. Rev. Lett.*, **96**, 201102
- Ott, C. D., Burrows, A., Dessart, L., & Livne, E. 2008, *ApJ*, **685**, 1069
- Ott, C. D., Burrows, A., Livne, E., & Walder, R. 2004, *ApJ*, **600**, 834
- Ott, C. D., Burrows, A., Thompson, T. A., Livne, E., & Walder, R. 2006b, *ApJS*, **164**, 130
- Ott, C. D., Dimmelmeier, H., Marek, A., Janka, H.-T., Hawke, I., Zink, B., & Schnetter, E. 2007, *Phys. Rev. Lett.*, **98**, 261101
- Qian, Y.-Z., & Woosley, S. E. 1996, *ApJ*, **471**, 331
- Rampp, M., & Janka, H.-T. 2002, *A&A*, **396**, 361
- Sato, J., Foglizzo, T., & Fromang, S. 2009, *ApJ*, **694**, 833
- Scheck, L., Janka, H.-T., Foglizzo, T., & Kifonidis, K. 2008, *A&A*, **477**, 931
- Shen, H., Toki, H., Oyamatsu, K., & Sumiyoshi, K. 1998, *Nucl. Phys. A*, **637**, 435
- Stevens, B. 2002, *Q. J. R. Meteorol. Soc.*, **128**, 2663
- Thompson, T. A., Burrows, A., & Meyer, B. S. 2001, *ApJ*, **562**, 887
- Thompson, T. A., Burrows, A., & Pinto, P. A. 2003, *ApJ*, **592**, 434
- Unno, W., Osaki, Y., Ando, H., Saio, H., & Shibahashi, H. 1989, *Nonradial oscillations of stars* (2nd ed.; Tokyo: Univ. Tokyo Press)
- van den Bergh, S., & Tammann, G. A. 1991, *ARA&A*, **29**, 363
- Wilson, J. R. 1985, in *Numerical Astrophysics*, ed. J. M. Centrella, J. M. Leblanc, & R. L. Bowers (Boston, MA: Jones and Bartlett), 422
- Woosley, S. E., & Heger, A. 2006, *ApJ*, **637**, 914
- Woosley, S. E., & Heger, A. 2007, *Phys. Rep.*, **442**, 269
- Woosley, S. E., Heger, A., & Weaver, T. A. 2002, *Rev. Mod. Phys.*, **74**, 1015
- Yamada, S., & Sato, K. 1995, *ApJ*, **450**, 245
- Yamasaki, T., & Foglizzo, T. 2008, *ApJ*, **679**, 607
- Yoshida, S., Ohnishi, N., & Yamada, S. 2007, *ApJ*, **665**, 1268
- Zwerg, T., & Müller, E. 1997, *A&A*, **320**, 209